INT. J. NUM. METH. HEAT FLUID FLOW, VOL. 2, 299–333 (1992)

A FINITE ELEMENT METHOD FOR CONDUCTION, INTERNAL RADIATION, AND SOLIDIFICATION IN A FINITE AXISYMMETRIC ENCLOSURE

S. BRANDON AND J. J. DERBY

Department of Chemical Engineering and Materials Science, University of Minnesota, Minneapolis, MN 55455, USA

ABSTRACT

A finite element method for the analysis of combined radiative and conductive heat transport in a finite axisymmetric configuration is presented. The appropriate integro-differential governing equations for a grey and non-scattering medium with grey and diffuse walls are developed and solved for several model problems. We consider axisymmetric, cylindrical geometries with top and bottom boundaries of arbitrary convex shape. The method is accurate for media of any optical thickness and is capable of handling a wide array of axisymmetric geometries and boundary conditions. Several techniques are presented to reduce computational overhead, such as employing a Swartz–Wendroff approximation and cut-off criteria for evaluating radiation integrals. The method is successfully tested against several cases from the literature and is applied to some additional example problems to demonstrate its versatility. Solution of a free-boundary, combined-mode heat transfer problem representing the solidification of a semitransparent material, the Bridgman growth of an yttrium aluminium garnet (YAG) crystal, demonstrates the utility of this method for analysis of a complex materials processing system. The method is suitable for application to other research areas, such as the study of glass processing and the design of combustion furnace systems.

KEY WORDS Internal radiation transport Swartz–Wendroff approximation Galerkin FEM

NOMENCLATURE

a	optical absorption coefficient
A, A*	Swartz–Wendroff geometric matrices (see Appendix D)
B, B*	Swartz–Wendroff geometric matrices (see Appendix D)
Bi_j	Biot number for $\partial D_j \equiv h_j R/k_s$, $(j = \mathrm{I}, \mathrm{II}, \mathrm{III})$
C, C*	Swartz–Wendroff geometric matrices (see Appendix D)
$\mathrm{d}S$	surface element $\equiv \mathrm{d}\tilde{S}/(2\pi R^2)$
$\mathrm{d}V$	volume element $\equiv \mathrm{d}\tilde{V}/(2\pi R^3)$
D	domain, where ∂D denotes domain boundary
$\mathbf{e}_x$	unit vector in direction x
E, E*	Swartz–Wendroff geometric matrices (see Appendix D)
F, F*	Swartz–Wendroff geometric vectors (see Appendix D)
G	furnace temperature gradient $\equiv (\tilde{T}_h - \tilde{T}_c)/L_A$
h	convective heat transfer coefficient
H	vertical position of interface $\equiv \tilde{H}/R$
i'	total directional radiative intensity $\equiv \tilde{i}'/(n^2\sigma\tilde{T}_0^4)$
J	Jacobian matrix

0961–5539/92/040299–35$2.00

Received September 1991
Revised February 1992

k thermal conductivity
$\mathbf{K}$, $\mathbf{K}^*$ Swartz–Wendroff geometric vectors (see Appendix D)
l radiative path length to boundary of participating medium $\equiv \tilde{l}/R$
L cylinder or ampoule length (dimensional)
L_A length of adiabatic zone (dimensional)
Lj minimum distance from (r, z) to boundary j $(j = 1, 2, 3)$, defined in Appendix C (dimensionless)
n refractive index
$\mathbf{n}$ unit vector pointing out of the participating medium
N conduction-to-radiation parameter $\equiv ka/(4n^2\sigma\tilde{T}_0^3)$
N_H number of finite element mesh nodes on ∂D_{ms}
N_a number of finite element mesh nodes on ∂D_d
N_T total number of nodes in finite element mesh
N_{Tb} number of finite element mesh nodes on ∂D_f
Pe dimensionless growth rate or Peclet number $\equiv \rho_c C_p V_g R/k_s$
$\mathbf{q}$ heat flux $\equiv \tilde{\mathbf{q}}/(n^2\sigma\tilde{T}_0^4)$
$\mathbf{q}_c$ conductive heat flux
$\mathbf{q}_R$ radiative heat flux
$\mathbf{q}_T$ total heat flux
Q heat generation $\equiv \tilde{Q}R/(n^2\sigma\tilde{T}_0^4)$
r radial coordinate $\equiv \tilde{r}/R$
R radius of medium
$\mathbf{R}$ vector of residual equations
Ra_j radiation number for $\partial D_j \equiv \varepsilon_0\sigma\tilde{T}_0^3 R/k_s$, $(j = \mathrm{I}, \mathrm{II}, \mathrm{III})$
S Stefan number $\equiv \Delta H_f/(C_p\tilde{T}_0)$
T temperature $\equiv T/T_0$
T_∞ effective sink temperature in (7)
$\tilde{T}_0$ reference temperature
V_g axial crystal growth rate
V_p ampoule velocity
$\mathbf{x}$ vector of unknowns in residual equations
y spatial variable shown in *Figure 5*
z axial coordinate $\equiv \tilde{z}/R$
z_A axial location of the adiabatic zone centre $\equiv \tilde{z}_A/R$

Greek symbols

α longitude (spherical coordinate)
β ratio of thermal conductivities $\equiv k_m/k_s$
Γ^i global quadratic basis function
γ^i local quadratic basis function
δ update vector
ΔH_f heat of fusion
ε emissivity
η local coordinate in *Figure 17*
θ colatitude (spherical coordinate)
θ_1 colatitude at the point where surface $b1$ meets surface $b3$
θ_2 colatitude at the point where surface $b2$ meets surface $b3$
κ optical path length as defined in (45)
Λ aspect ratio $\equiv R/L$
ρ density
ξ local coordinate in *Figure 17*

σ Stefan–Boltzmann constant
τ dimensionless absorption coefficient, or optical thickness $\equiv aR$
τ^* rescaled optical thickness $\equiv \tau/\Lambda$
ϕ polar angle (cylindrical coordinate)
ϕ_z polar angle shown in *Figure 5a* and defined in (33)
Φ^i global biquadratic basis function
ϕ^i local biquadratic basis function
ψ angle between direction of intensity and normal to surface
Ω solid angle

Mathematical symbols

∇ gradient operator $\equiv \mathbf{e}_r\,\partial/\partial r + \mathbf{e}_z\,\partial/\partial z$ for axisymmetric geometry
$\cdot$ dot product
$\|\cdot\|_2$ L-2 norm

Subscripts

b evaluated at system boundary
c cold
d Dirichlet boundary condition is applied
f flux boundary condition is applied
fu furnace
h hot
i inner surface
m melt
mp melting point
ms evaluated at melt/crystal interface
r, z components in coordinate directions
s solid
o outer surface
1 evaluated within the bottom segment of meridional plane ($\theta \geqslant \theta_1$)
2 evaluated within the top segment of meridional plane ($\theta \leqslant \theta_2$)
3 evaluated within the middle segment of meridional plane ($\theta_2 < \theta < \theta_1$)
I evaluated at ampoule bottom, ∂D_{I}
II evaluated at ampoule top, ∂D_{II}
III evaluated at ampoule periphery, $\partial D_{\mathrm{III}}$

Superscripts

(i) finite element interpolant
k iteration counter
$\tilde{}$ dimensional unknown or coordinate

INTRODUCTION

The transport of heat via radiation within a participating medium (commonly referred to as internal radiative transport) is significant in many industrial processes, such as combustion, glass technology and high temperature crystal growth. The need for better understanding and design of such systems necessitates the incorporation of internal radiative effects into global heat transfer models of these processes. However, this introduces significant complications, both in

terms of model formulation and in terms of solution strategies. In the most general case, the problem is described by the radiative transport equation coupled with the equation of change of energy, leading to a multi-dimensional integro-differential equation[1].

Analytical solutions to radiative transport problems are available only for a few simple cases, and for most geometries and boundary conditions of practical interest, one must resort to numerical solution techniques. These include Hottel's zone method, P–N approximation techniques, the discrete ordinates method, Monte Carlo methods, and others[1–4]. An overview of prior research in radiative heat transport, as well as a review of current solution techniques, is given by Howell[2]. A more detailed description of various numerical methods is found in a review by Chan[3], and Viskanta and Mengüç[4] discuss the application of several methods in the context of combustion furnace modelling.

In this study, we present a novel finite element formulation for multi-dimensional internal radiation problems; we detail prior research using the finite element method later in this section. We are specifically concerned with several problems which are characterized by cylindrical geometries. Most early analyses of radiative transport concerned plane-parallel geometries of interest to astrophysics[5–7] and preliminary studies by the heat transfer community[8–10]. Comparatively few studies have considered more complicated geometries.

Many early analyses of cylindrical geometries considered one-dimensional problems of pure radiation (i.e. no conduction or convection). For example, Perlmutter and Howell[11] applied the Monte Carlo technique to the problem of absorption, emission, and uniform heat generation in a grey gas trapped between grey and diffuse concentric cylinders. Kesten[12] formulated the exact integral equation for the radial radiative flux for a prescribed temperature profile in a grey medium contained within a black-walled, infinite cylinder.

Two- and three-dimensional formulations were considered by Dua and Cheng[13] and Crosbie and Farrell[14]. Both studies obtained analytical expressions for the radiation field accompanying prescribed temperature distributions across cylindrical enclosures containing grey participating media. In addition, Crosbie and Farrell accounted for anisotropic scattering and investigated several radiation boundary conditions. Lin[15] formulated expressions for radiative fluxes and source functions in various geometries. His formulations for cylindrical geometries were disputed by Thynell[16], who later applied his own expressions to the problem of radiation in a grey, participating, and isotropically scattering medium in a finite cylinder with grey and diffuse walls[17]. Siegel[18,19] formulated and solved the problem of transient cooling of an absorbing, emitting, and scattering cylinder in a study of waste heat dissipation from power plants in outer space via radiative transport.

Studies which consider combined conduction and radiation in cylindrical geometries are not so abundant. Kim and Smith[20] used the zone method to study radiation and conduction in a finite cylinder with grey and diffuse walls. Results were shown for cases where prescribed wall temperatures were given (Dirichlet boundary conditions), as well as prescribed fluxes on the side wall (flux boundary conditions). This approach was extended by Al-Turki and Smith[21], who modelled the interaction of radiation, conduction, and convection (fully developed laminar or turbulent velocity profiles were assumed *a priori*), in a furnace containing a soot/gas mixture. Tabanfar and Modest[22] considered conduction, convection, and radiation in a black-walled axisymmetric cylinder. The method of discrete ordinates, coupled with finite differences, was applied by Yücel and William[23] to the analysis of heat transfer in a grey, emitting, absorbing and scattering finite cylinder. One-dimensional studies of heat transfer in a participating and conducting medium trapped between infinite, concentric black cylinders were presented by Pandey[24] and Harris[25].

The finite element method (FEM) was applied to neutron transport problems in the early 1970s (see, for example Reference 26); however, even though the transport equations are essentially identical, the use of finite element methods to solve for radiative transport in participating media has occurred only fairly recently. Wu *et al.*[27] and Fernandes *et al.*[28,29] applied the Galerkin FEM to the problem of heat transfer in a grey, absorbing, emitting,

conducting and isotropically scattering medium trapped between infinite grey and diffuse parallel plates. Razzaque *et al.* were the first to apply the Galerkin FEM to the two-dimensional problem of pure radiation in a participating medium[30] and combined radiation and conduction in a rectangular enclosure with grey walls[31]. The Galerkin FEM was also employed by Chung and Kim[32] in their study of combined radiation, conduction and convection in two-dimensional flow through a converging or diverging region between two plates.

Dombrovskii and Barkova[33] developed a finite element scheme for the solution of the radiative transport equation. Their method, which is based on the expansion of the intensity in linear basis functions, was applied to two different problems of two-dimensional radiant heat transfer in an anisotropically scattering, flowing gas/particle mixture. A hybrid Monte Carlo/FEM algorithm was developed by Kraus[34]. The radiative term in the equation of change of energy was computed using a Monte Carlo (MC) algorithm, while the equation itself was solved (with the MC input) using the Galerkin FEM with bilinear elements. Recently, Saltiel and Naraghi[35] suggested that their method, based on discrete exchange factors, would be highly compatible with finite element meshes, thus simplifying calculations in complex geometries.

Our development of finite element methods stems from the interest we have in the role of radiative transport during the growth of single crystals from the melt, which is important in many oxide systems such as yttrium aluminium garnet (YAG) and sapphire (see Refs. 36–39 for more details). The FEM has been successfully employed in the past to solve free-boundary transport problems with irregular domain geometries and complicated boundary conditions associated with crystal growth processes[40]. However, most of the reported theoretical studies were not concerned with semitransparent crystals. Derby *et al.*[41] give a comprehensive analysis of the Czochralski growth of oxide crystals, but did not include internal radiative effects in their study. A greatly simplified two-band radiation transport model in which one wavelength band is completely transparent and the other completely opaque was used by Crochet and co-workers[42,43] and by Thomas *et al.*[44] in their studies of large scale crystal growth systems.

The effects of internal radiative heat transport in semitransparent crystal growth have been studied by various authors using one-dimensional models of conduction and radiation for highly idealized geometries[45,46] and for growth configurations which produce very long, thin crystals[47,48]. In addition there has been some prior work with simplified two-dimensional models. An optically thick approximation (P_1) was employed by Kim and Yimer[49], who studied solidification in a finite annular region. The same approach (P_1) was taken by Matsushima and Viskanta[50] in their study of combined radiation, conduction and convection in a two-dimensional crystal growth configuration. They accounted for spectral effects, but did not account for the shape and position of the melt/crystal interface, which was fixed *a priori*. More recently, we have applied the method described in this study to solve the problem of quasi-steady-state crystal growth in the vertical Bridgman configuration, calculating the effects of an emitting, absorbing and conducting solid phase along with the determination of the melt/crystal interface position[36].

FORMULATION

In this section, we pose two model problems which involve energy transport through participating media. The first problem concerns heat transfer through a finite axisymmetric enclosure containing a participating medium and demonstrates the power of the finite element method to accurately calculate temperature fields for a variety of parameters and boundary conditions. The techniques developed for this problem have also been successfully applied to describe heat transfer and fluid flow in a Rayleigh–Bénard system which features a radiatively participating fluid[51]. The second problem is of more practical interest and describes the solidification of a semitransparent crystal. Further results for this system are reported in References 36 and 37. In the ensuing discussion, we present the governing equations and follow with the formulation of our model problems.

A radiatively participating medium absorbs, emits, and scatters infra-red radiation. We consider here a non-scattering medium with optical properties which are temperature-independent and grey (wavelength-independent) in which both conduction heat transfer and radiative processes are significant. The dimensionless form of the steady-state governing equation of energy within the medium is:

$$-\nabla\cdot\left(\frac{4N}{\tau}\nabla T\right)+\nabla\cdot\mathbf{q}_R=0 \tag{1}$$

where ∇ is the gradient operator, N is the conduction-to-radiation parameter, τ is the dimensionless optical absorption coefficient or the optical thickness of the medium, T is temperature, and $\mathbf{q}_R$ is the radiative energy flux vector. The divergence of the radiative flux vector is given by:

$$\nabla\cdot\mathbf{q}_R=\tau\left[4T^4-\int_{\Omega=0}^{4\pi} i'(\Omega)\,\mathrm{d}\Omega\right] \tag{2}$$

where i' is the total directional radiative intensity and Ω is the solid angle. All variables and dimensionless groups are defined in the Nomenclature section.

The total directional radiative intensity is represented by the integrated form of the radiative transfer equation[1]:

$$i'(\Omega)=i'(\Omega,0)\exp[-\tau l(\Omega)]+\frac{\tau}{\pi}\int_0^l T^4(l^\dagger)\exp[-\tau(l-l^\dagger)]\,\mathrm{d}l^\dagger \tag{3}$$

where $i'(\Omega)$ is the radiation intensity evaluated at a certain point within the domain and directed along the solid angle Ω, l is the distance from the domain boundaries along the solid angle Ω, and $l^\dagger$ is a dummy variable of integration. The first term on the right-hand-side of the equation represents radiative intensity coming into the medium from the system boundaries, while the second term accounts for incoming radiation emitted from the intervening media between the point at which i' is evaluated and the boundaries.

The boundary radiation intensity, $i'(\Omega,0)$ in the above equation, must satisfy the following condition. For diffuse and grey boundaries, the intensity directed towards the interior of the domain is:

$$i'(\Omega,0)=\frac{1}{\pi}\left\{T_b^4-\frac{1-\varepsilon_i}{\varepsilon_i}[\mathbf{q}_R\cdot(-\mathbf{n}_b)]\right\} \tag{4}$$

where T_b represents the temperature of the boundary, ε_i is the emissivity of the inner surface of the domain, and $\mathbf{q}_R\cdot(-\mathbf{n}_b)$ is the net radiative flux into the domain at its boundary. The boundary temperature T_b is taken throughout this study to represent both the temperature of the wall and the temperature of the medium at the boundary. This must always be true as long as any conduction heat transfer is present. However, if only radiative transport is considered, there can be a discontinuity between the temperature of the medium and that of the adjacent boundary, giving rise to the phenomenon referred to as radiation temperature slip.

Substitution of (2)–(4) into (1) gives rise to an integro-differential energy balance equation. Boundary conditions are presented in the following two sections for the model problems considered here. In a subsequent section, the specific procedures employed to solve these problems are discussed.

Participating medium in an axisymmetric enclosure

For this model problem, we consider a finite, uniform-radius, axisymmetric domain with an arbitrarily shaped, convex (with respect to the medium) top and bottom (see *Figure 1*). The domain contains a thermally conducting, semitransparent material with grey and

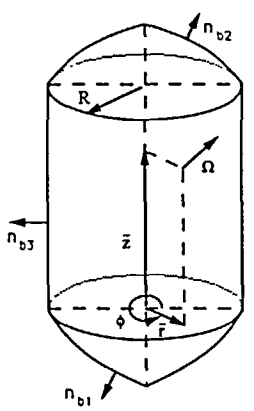

Figure 1 Our formulation is for an axisymmetric geometry of uniform radius with arbitrarily shaped, convex top and bottom

temperature-independent properties. Convective transport is neglected, as is the scattering of radiation. The boundaries and grey and diffuse.

We consider boundary conditions for the temperature field which are both general and physically significant. Dirichlet conditions are imposed along one part of the boundary (denoted ∂D_d),

$$T = T_b(r, z) \tag{5}$$

and energy flux conditions are imposed along the remainder of the system boundary (denoted ∂D_f)

$$\left(-\frac{4N}{\tau}\nabla T + \mathbf{q}_R\right)\cdot\mathbf{n}_b = \mathbf{q}_b\cdot\mathbf{n}_b \tag{6}$$

where the subscript b denotes a boundary property and $\mathbf{n}_b$ is an outward-pointing unit vector normal to the system boundaries (see *Figure 1*). The flux $\mathbf{q}_b$ in (6) is usually represented by one of the following forms:

$$\mathbf{q}_b\cdot\mathbf{n}_b = \begin{cases} 0 & \text{adiabatic} \\ \dfrac{4N}{\tau}Bi(T_b - T_\infty) & \text{Newton's law of cooling} \\ \dfrac{4N}{\tau}Ra(T_b^4 - T_\infty^4) & \text{radiating} \end{cases} \tag{7}$$

where Bi is a dimensionless heat transfer coefficient, the Biot number and Ra is a dimensionless surface radiation heat transfer coefficient, sometimes referred to as the Radiation number. Both of these parameters refer to energy transport outward from the domain surface.

The last two conditions of (7) are often summed to represent a boundary which is losing heat via combined convection and radiation. Note that for the radiative cooling of a surface, we employ the convention of an effective sink temperature, T_∞. To accurately describe surface interactions in a radiative enclosure filled with a non-participating medium, this parameter must take into account geometric factors, surface emissivities and temperatures (e.g. through the use of Gebhart's method[52]).

We will consider axisymmetric temperature distributions which additionally require that, along the centreline of the system,

$$\mathbf{q} \cdot (-\mathbf{e}_r)|_{r=0} = 0 \tag{8}$$

where $\mathbf{e}_r$ is a unit basis vector oriented in the radial direction.

Solidification within a cylindrical ampoule

The second problem considered in this study represents the growth of a semitransparent crystal in a vertical Bridgman system. This model is applicable to the high-temperature melt growth of many refractory crystals, such as sapphire and yttrium aluminium garnet (YAG). We describe below our model system.

An axisymmetric cylindrical ampoule containing both crystalline and molten phases travels slowly (characteristic translation rates are on the order of 1 mm/h) downward through the cylindrical bore of a furnace. The ampoule moves from a hot zone (with constant temperature $T = T_h$) through an adiabatic zone to an isothermal cold zone ($T = T_c$). The furnace wall temperature in the adiabatic zone is approximated by a linear drop between T_h and T_c. A schematic diagram of this system and its mathematical representation are shown in *Figure 2*.

We consider combined radiative and conductive transport in the solid crystalline phase, while conduction alone is assumed to dominate heat transfer through the melt. Since the translation rate is very small, we apply a quasi-steady-state analysis. This approach assumes that the local axial solidification velocity is everywhere equal to the ampoule translation rate and that the time scale for heat transfer through the system is fast enough so that all transients can be ignored and the steady-state heat transfer equations are applicable. In addition, the ampoule is considered to be vanishingly thin and is therefore ignored in the heat transfer analysis. (The effects of the ampoule on heat transfer are considered elsewhere[37].)

Boundary conditions account for natural convection combined with enclosure radiation heat

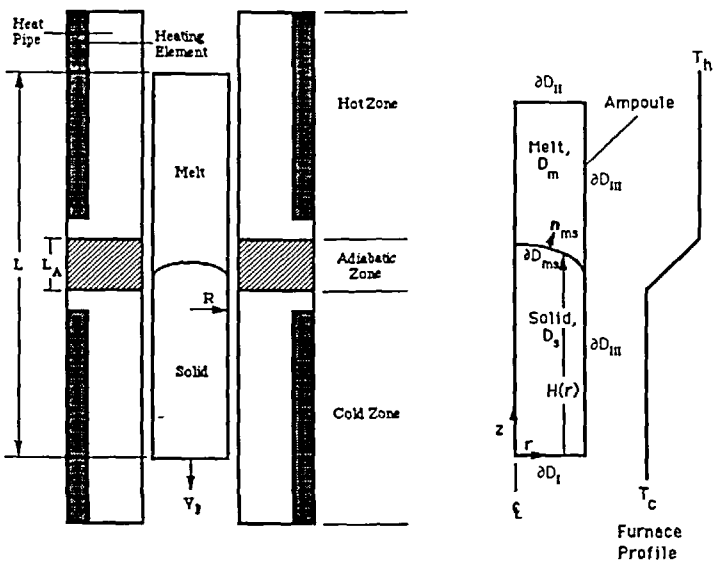

Figure 2 Model vertical Bridgman system for growth of semitransparent crystals. (a) Schematic diagram of system. (b) Mathematical description

transfer between the ampoule and interior furnace bore:

$$\mathbf{q}\cdot(-\mathbf{e}_z)|_{z=0} = \frac{4N}{\tau}[Bi_{\mathrm{I}}(T - T_c) + Ra(T^4 - T_c^4)] \tag{9}$$

$$\mathbf{q}\cdot\mathbf{e}_z|_{z=\Lambda^{-1}} = \frac{4N}{\tau}[Bi_{\mathrm{II}}(T - T_h) + Ra(T^4 - T_h^4)] \tag{10}$$

$$\mathbf{q}\cdot\mathbf{e}_r|_{r=1} = \frac{4N}{\tau}[Bi_{\mathrm{III}}(T - T_{fu}(z)) + Ra(T^4 - T_{fu}^4(z))] \tag{11}$$

where the three Biot numbers account for different heat transfer coefficients, $T_{fu}(z)$ represents the furnace temperature profile and $\Lambda \equiv R/L$ is the aspect ratio of the ampoule. In formulating these boundary conditions, we have assumed that the ampoule is close enough to the furnace walls so that the effects of the enclosure geometry are not important and the ampoule exchanges heat directly with the adjacent furnace wall.

The melt/crystal interface is a free boundary in this model; its position and shape are not set *a priori* but are determined along with the temperature field of the system. Two conditions must be satisfied along the melt/crystal interface. The isotherm condition prescribes that the solidification front (described by $z = H(r)$) fall along the melting-point isotherm of the system,

$$T(r, H(r)) = T_{mp} \tag{12}$$

where T_{mp} is the melting temperature of the material. The second condition consists of a simple energy balance, taking into account the energy fluxes across the interface and the release of latent heat at the interface,

$$(\mathbf{q}_m\cdot\mathbf{n}_{ms} - \mathbf{q}_s\cdot\mathbf{n}_{ms})|_{z=H(r)} = \frac{4N}{\tau}PeS(\mathbf{e}_z\cdot\mathbf{n}_{ms}) \tag{13}$$

where $\mathbf{q}_m$ and $\mathbf{q}_s$ are heat fluxes in the melt and solid phases, respectively, $\mathbf{n}_{ms}$ is a unit vector normal to the interface directed at the melt, Pe is a dimensionless growth rate, here expressed as a Peclet number, and S is the Stefan number, which is a dimensionless latent heat.

As in the previous problem, axisymmetry requires that

$$\mathbf{q}\cdot(-\mathbf{e}_r)|_{r=0} = 0 \tag{14}$$

METHODOLOGY

In the following section, we describe the general approach to solving the integro-differential heat balance equation (1) using the Galerkin finite element method (GFEM) and the Newton–Raphson iteration scheme. Of particular importance for combined mode heat transfer problems is the accurate evaluation of the integrals which arise in the radiative flux terms of (1).

Numerical solution: GFEM and Newton–Raphson iterative method

The Galerkin finite element method provides the framework for solving both model problems. This choice of methodology was motivated by the self-consistent manner in which realistic boundary conditions and complex geometries are implemented. The domain of interest is discretized into a two-dimensional mesh of elements in the plane $\phi = 0$, and the temperature field is expanded by a C^0 finite element basis set defined by this mesh[54],

$$T(r, z) = \sum_{i=1}^{N_T} T^{(i)}\Phi^i(r, z) \tag{15}$$

where $T(r, z)$ is the dimensionless temperature field defined over our axisymmetric domain, N_T is the total number of nodes in the finite element mesh, $\{T^{(i)}\}$ are unknown coefficients in the expansion which represent the temperature at each node, and $\{\Phi^i(r, z)\}$ are the piecewise-continuous basis functions. We employ nine-node quadrilateral Lagrangian basis functions for all of the calculations reported here.

The Galerkin weighted residual equations are obtained by multiplying the field equation (1) by the basis functions, $\{\Phi^i(r, z)\}$ for $i = 1, \ldots, N_T$, and integrating over the problem domain D,

$$\int_D \Phi^i(r, z)\left[-\nabla\cdot\left(\frac{4N}{\tau}\nabla T\right) + \nabla\cdot\mathbf{q}_R\right] dV = 0 \tag{16}$$

The divergence theorem is then applied to these weighted residuals, yielding the weak form of the equation set,

$$\int_{\partial D} \Phi^i(r, z)\left[\left(-\frac{4N}{\tau}\nabla T + \mathbf{q}_R\right)\cdot\mathbf{n}_b\right] dS - \int_D \nabla\Phi^i(r, z)\cdot\left(-\frac{4N}{\tau}\nabla T + \mathbf{q}_R\right) dV = 0 \tag{17}$$

where ∂D denotes the surface surrounding the domain and $\mathbf{n}_b$ is an outward-pointing unit normal.

The application of the divergence theorem to both terms of (16), resulting in the weak form given above, has not been used in prior multi-dimensional calculations[31–34]. (Fernandes *et al.*[29] employed this formulation for a one-dimensional problem but did not use it in an earlier study[28].) However, this form of the equation set is particularly advantageous to employ. The first term of the equation allows for a natural implementation of various energy flux boundary conditions. The second term of (17) contains components of the radiative flux vector itself rather than the divergence of the flux vector; this simplification will be further discussed in the following section.

Boundary conditions for the temperature field are imposed in the following manner. For the flux boundary conditions along ∂D_f, the kernel of the surface integral in (17) is replaced by the desired form from (6) and (7). Over portions of the domain boundary where Dirichlet conditions apply (∂D_d), the appropriate residual equations from (17) are replaced by essential conditions, resulting in the boundary nodal temperature values simply being specified by the conditions from (5).

To make the original integro-differential heat balance equation (1) well posed, the boundary term $i'(\Omega, 0)$ of the integrated radiative transfer equation (3) must be specified. This is easily accomplished for portions of the system boundaries where flux conditions are specified. A heat balance along ∂D_f yields an explicit equation for the radiative flux at the boundary,

$$\mathbf{q}_R\cdot(-\mathbf{n}_b) = \left(\frac{4N}{\tau}\nabla T + \mathbf{q}_b\right)\cdot(-\mathbf{n}_b) \tag{18}$$

where both terms on the right-hand-side of the equation can be determined directly from the temperature field—the first term is obtained by differentiating the finite element representation of the temperature field, (15), and the second term is given directly by (7). Equation (18) is used in conjunction with (4) to specify $i'(\Omega, 0)$.

No explicit form exists for boundaries where Dirichlet conditions are imposed, since the total heat flux from the boundary $\mathbf{q}_b\cdot(-\mathbf{n}_b)$ depends on both the conductive and radiative fluxes. Instead, we consider the following balance for the net radiative energy flux into the domain at its boundary,

$$\mathbf{q}_R\cdot(-\mathbf{n}_b) = \varepsilon_i\left[T_b^4 - \int_{\Omega=0}^{2\pi} i'(\Omega)\cos(\psi_b)\, d\Omega\right] \tag{19}$$

In this equation $i'(\Omega)$ is integrated over a hemisphere surrounding the point of interest on the boundary. This integration accounts for the directional intensity of radiation emitted from within the domain (and its boundaries) towards this point of interest (see *Figure 3*). The quantity ψ_b is determined by the angle between the outward pointing normal to the surface $\mathbf{n}_b$ and the

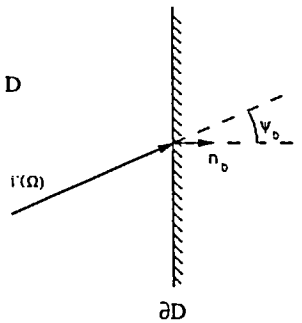

Figure 3 Directional radiative intensity $i^i(\Omega)$ impinging on a portion of the system boundary at an angle of ψ_b

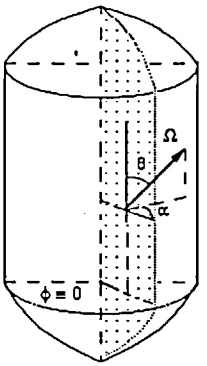

Figure 4 The localized spherical coordinate system at a point in the plane of $\phi = 0$. Longitude α and colatitude θ are also indicated for the point

direction in which the intensity is directed. Along ∂D_d, we represent the net radiative flux into the system at the boundary with a finite element expansion,

$$[\mathbf{q}_R \cdot (-\mathbf{n}_b)](x) = \sum_{i=1}^{N_q} q^{(i)} \Gamma^i(x) \tag{20}$$

where N_q is the number of nodes on the part of the boundary where the Dirichlet condition is applied (∂D_d), x is the surface coordinate, and $q^{(i)}$ represents the interpolated values of the net radiative flux into the system at each surface node. For this study, we use one-dimensional Lagrangian quadratic basis functions for this expansion. We then form Galerkin residual equations by multiplying (19) by the basis functions, $\{\Gamma^i\}$ for $i = 1, \ldots, N_q$, and integrating over the appropriate portions of the boundary,

$$\int_{\partial D_d} \Gamma^i \left\{ [\mathbf{q}_R \cdot -(\mathbf{n}_b)] - \varepsilon \left[T_b^4 - \int_{\Omega=0}^{2\pi} i^i(\Omega) \cos(\psi_b)\, d\Omega \right] \right\} dS = 0 \tag{21}$$

The surface radiative fluxes determined by these equations are then used in (4) to calculate $i^i(\Omega, 0)$.

Equations (17), appropriately modified for the desired boundary conditions, and, if Dirichlet conditions are employed, equations (21) are evaluated by substituting the finite element approximations for the temperature field (15) and radiative boundary fluxes (20) into these integral equations and computing their values by Gaussian quadrature. Nine-point quadrature was used for all volume integrals, and three-point quadrature was employed to evaluate all surface integrals. More details of this procedure, especially with regard to the radiative terms, are provided in the next section. This procedure results in a non-linear algebraic equation set for the coefficients $\{T^{(i)}\}$ and $\{q^{(i)}\}$. This set is conveniently expressed as:

$$\mathbf{R}(\mathbf{x}) = 0 \tag{22}$$

where $\mathbf{x} \equiv (T^{(1)}, T^{(2)}, \ldots, T^{(N_T)}, q^{(1)}, q^{(2)}, \ldots, q^{(N_q)})^T$ is a vector of dimension $N_T + N_q$.

The Newton–Raphson method is used to solve this set of equations. An initial guess for the vector of unknowns is made, $\mathbf{x}^{(0)}$, and successive updates to the unknowns vector are computed using the following iterative scheme:

$$\mathbf{x}^{(k+1)} = \mathbf{x}^{(k)} + \delta^{(k)} \tag{23}$$

where k is the iteration counter. The update vector $\delta^{(k)}$ is generated by solution of the linear equations

$$\mathbf{J}(\mathbf{x}^{(k)})\delta^k = -\mathbf{R}(\mathbf{x}^{(k)}) \tag{24}$$

where $J_{ij} = \partial R_i/\partial x_j$ are elements of the Jacobian matrix. Closed-form expressions are used to calculate most of the Jacobian elements; however, we resort to numerical approximations for those whose analytical form is intractable (typically due to complications from the radiation integrals). Further details are presented in ensuing sections. The iterations are continued until the $L-2$ norm of the update vector $\delta^{(k)}$ is smaller than some specified criterion, e.g. $\|\delta^{(k)}\|_2 < 10^{-7}$. Typically, 4–7 iterations are required until convergence is achieved.

The linear equation set (24) is solved directly via LU decomposition. Unlike the banded Jacobian matrix structures which typically arise during GFEM solutions to conventional heat transfer problems, the Jacobian matrices for the problems considered in this study are dense due to long-range radiative interactions through the participating medium. This increases the time required for the solution of (24). However, this is not an important issue since calculation of the radiative terms dominates the overall CPU time requirements, as is further discussed in the Results section.

When the method is applied to a solidification problem one must also account for the free boundary (melt/crystal interface, $z = H(r)$) whose position is not known *a priori*. This significantly complicates the analysis, which now involves the expansion of the interface position in a one dimensional quadratic basis set,

$$H(r) = \sum_{i=1}^{N_H} H^{(i)}\Gamma^i(r) \tag{25}$$

where N_H is the number of nodes on the interface. The extra set of unknowns which track the solidification front ($\{H^{(i)}, i = 1, \ldots, N_H\}$) are determined via the isotherm method, as described by Ettouney and Brown[53]. The mesh deforms from one Newton iteration to the next until the converged mesh conforms to the correct shape and position of the interface for a given steady-state solution. This renders the cost saving Swartz–Wendroff approximation (described below) ineffective. We have therefore abandoned the approximation for this problem and have solved the rigorous form of the radiation terms. In addition, all terms of the Jacobian matrix were calculated in closed-form, except for the derivatives of the components of the radiative flux ($\mathbf{q}_R\cdot\mathbf{e}_r$ and $\mathbf{q}_R\cdot\mathbf{e}_z$) with respect to the interface position $\{H^{(i)}, i = 1, \ldots, N_H\}$. These entries were calculated numerically using a first-order finite difference approximation, with a perturbation in the value of $H^{(i)}$ on the order of 10^{-8}–10^{-10}.

Evaluation of the radiative energy flux

The accurate evaluation of the radiative terms in (17) is one of the most important and difficult aspects of combined-mode heat transfer problems. In the following discussion, we address these issues with respect to the geometry of the first model problem. Although these equations are also applicable to the crystal growth problem (the crystalline phase is considered to be a participating medium), their specific form will be somewhat different.

As shown above in the weak formulation of the residuals, only the components of the radiative flux vector, namely $\mathbf{q}_R\cdot\mathbf{e}_r$ and $\mathbf{q}_R\cdot\mathbf{e}_z$, need be computed rather than the divergence of the radiative flux vector, $\nabla\cdot\mathbf{q}_R$. The radiative flux through any mathematical surface within the domain is given by:

$$\mathbf{q}_R\cdot\mathbf{e}_x = \int_{\Omega=0}^{4\pi} i'(\Omega)\cos(\psi_x)\,\mathrm{d}\Omega \tag{26}$$

where x represents the direction normal to the surface, $i'(\Omega)$ is the radiation intensity as defined in (3), and ψ_x is the angle between $i'(\Omega)$ and the normal to the surface.

Although the temperature field is assumed to be axisymmetric, the radiation intensity depends on the three-dimensional geometry of the entire enclosure. Fortunately, some simplifications from symmetry are possible. The axisymmetry of the system allows us to solve for the temperature field in a manner which is independent of the polar angle ϕ. As shown in *Figure 4*, we choose to evaluate the problem in a plane of constant ϕ, which for convenience is taken as $\phi = 0$.

As mentioned previously, nine-point and three-point Gaussian quadrature is used to evaluate the volume and surface integrals in the residual equations (17) and (21). These quadrature points (or Gauss points) lie on the $\phi = 0$ plane shown in *Figure 4*. At these particular points, we must evaluate radiative terms given by (26). This is most readily accomplished by defining local spherical coordinate systems at each Gauss point.

The local spherical coordinate system at one such point is illustrated in *Figure 4*. The colatitude θ is well defined with respect to the z-axis of the system, while the longitude α is positioned such that $\alpha = 0$ corresponds to $\phi = 0$. As a result of the axisymmetry of the system, it is sufficient to consider α values of 0 to π. The colatitude θ also spans the same angles, 0 to π. A view of the system from above is shown in *Figure 5a*, while *Figure 5b* describes a cut through the domain at a constant α value. The coordinates (r, z) in *Figure 5b* mark the origin of this coordinate system (the location of the Gauss point).

A solid angle increment in this localized coordinate system is given by:

$$d\Omega = \sin(\theta)\, d\theta\, d\alpha \tag{27}$$

and (26) becomes:

$$\mathbf{q}_R(r, z)\cdot\mathbf{e}_x = 2\int_0^{\pi}\int_0^{\pi} i'(\theta, \alpha; r, z)\cos[\psi_x(\theta, \alpha; r, z)]\sin(\theta)\, d\theta\, d\alpha \tag{28}$$

A natural splitting of this integral produces three regions with respect to values of the θ coordinate: $\theta = 0$ to θ_2, $\theta = \theta_2$ to θ_1, and $\theta = \theta_1$ to π, see *Figure 5b*.

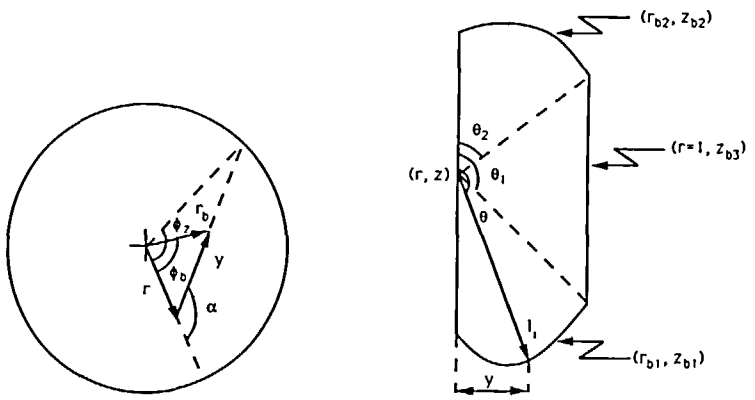

Figure 5 Further details of the problem domain. (a) View from above, for the specific case of $\theta > \theta_1$ or $\theta < \theta_2$. Point r_b lies along the top or bottom surface; variable y is employed for some problem integrals. (b) A plane of constant α viewed from the side, for the specific case of $\theta > \theta_1$. Point (r, z) indicates origin of local coordinate system (Gauss point for GFEM residuals)

Applying this splitting along with substitution from (3) and (4), (28) becomes:

$$\begin{aligned}\mathbf{q}_R(r,z)\cdot\mathbf{e}_x = \frac{2}{\pi}\int_0^{\pi}\Bigg\{\int_{\theta_1(z)}^{\pi}\left[T_{b1}^4 - \frac{1-\varepsilon_{i1}}{\varepsilon_{i1}}\mathbf{q}_R\cdot(-\mathbf{n}_{b1})\right]\exp(-\tau l_1)\cos(\psi_{x1})\sin(\theta)\,\mathrm{d}\theta \\ + \int_0^{\theta_2(z)}\left[T_{b2}^4 - \frac{1-\varepsilon_{i2}}{\varepsilon_{i2}}\mathbf{q}_R\cdot(-\mathbf{n}_{b2})\right]\exp(-\tau l_2)\cos(\psi_{x2})\sin(\theta)\,\mathrm{d}\theta \\ + \int_{\theta_2(z)}^{\theta_1(z)}\left[T_{b3}^4 - \frac{1-\varepsilon_{i3}}{\varepsilon_{i3}}\mathbf{q}_R\cdot(-\mathbf{e}_r)|_{b3}\right]\exp(-\tau l_3)\cos(\psi_{x3})\sin(\theta)\,\mathrm{d}\theta \\ + \tau\Bigg[\int_{\theta_1(z)}^{\pi}\int_0^{l_1} T^4(l_1^{\dagger})\exp[-\tau(l_1-l_1^{\dagger})]\,\mathrm{d}l_1^{\dagger}\cos(\psi_{x1})\sin(\theta)\,\mathrm{d}\theta \\ + \int_0^{\theta_2(z)}\int_0^{l_2} T^4(l_2^{\dagger})\exp[-\tau(l_2-l_2^{\dagger})]\,\mathrm{d}l_2^{\dagger}\cos(\psi_{x2})\sin(\theta)\,\mathrm{d}\theta \\ + \int_{\theta_2(z)}^{\theta_1(z)}\int_0^{l_3} T^4(l_3^{\dagger})\exp[-\tau(l_3-l_3^{\dagger})]\,\mathrm{d}l_3^{\dagger}\cos(\psi_{x3})\sin(\theta)\,\mathrm{d}\theta\Bigg]\Bigg\}\,\mathrm{d}\alpha \end{aligned} \tag{29}$$

where l_j $(j = 1, 2, 3)$ is the ray length between the point (r, z) and a point on one of the boundaries (r_{bj}, z_{bj}). The net radiative fluxes into the system at the boundaries, $\mathbf{q}_R\cdot(-\mathbf{n}_{b1})$, $\mathbf{q}_R\cdot(-\mathbf{n}_{b2})$, and $\mathbf{q}_R\cdot(-\mathbf{e}_r)|_{b3}$ are available using (18) along ∂D_f or solving (21) along ∂D_d. The specific form of the surface fluxes (19) along the Dirichlet boundary are presented in Appendix A.

The direction cosines of (29) are, in the case of $\mathbf{e}_x = \mathbf{e}_r$,

$$\cos(\psi_{rj}) = -\sin(\theta)\cos(\alpha) \quad j = 1, 2, 3 \tag{30}$$

and, for $\mathbf{e}_x = \mathbf{e}_z$,

$$\cos(\psi_{zj}) = -\cos(\theta) \quad j = 1, 2, 3 \tag{31}$$

The integration limits, $\theta_1(\alpha)$, $\theta_2(\alpha)$ are calculated by,

$$\theta_j(\alpha) = \begin{cases} \arctan\left\{\dfrac{1}{[z_{bj}(r=1)-z]}\dfrac{\sin\phi_z}{\sin\alpha}\right\} & z < z_{bj}(r=1) \\ \pi - \arctan\left\{\dfrac{1}{[z-z_{bj}(r=1)]}\dfrac{\sin\phi_z}{\sin\alpha}\right\} & z > z_{bj}(r=1) \end{cases} \tag{32}$$

where

$$\phi_z = \alpha - \arcsin(r\sin(\alpha)) \tag{33}$$

and $j = 1, 2$.

To speed the evaluation of the integrals of (29), the variables of integration must be chosen so that all quantities in the integrands can be evaluated explicitly. This is achieved through the choice of the longitude α and the dummy variable $l_j^{\dagger}$, $(j = 1, 2, 3)$ as two of the three variables of integration. In terms where $j = 3$ (i.e. terms which view the side wall, $\theta_2(\alpha) < \theta < \theta_1(\alpha)$), the colatitude θ is an acceptable third variable of integration. However, all integrand quantities are not explicit when $j = 1, 2$ (terms which view either end of the enclosure), so a new variable of integration $y(\theta)$ is defined, see *Figure 5*. The expressions that relate the known variables (y or θ, α, $l_j^{\dagger}$, etc.) to the unknown quantities needed for the evaluation of (29)–(32) are given in Appendix B.

A repeated discretization with Gauss–Legendre quadrature is employed for the evaluation of the solid angle and line integrals in (29) and (21). Fidelity to the GFEM would require all solid angle integrals and line integrals to be evaluated element-by-element since the representation

of the temperature field and the finite element isoparametric mappings are only piecewise differentiable. However, it is much more efficient to evaluate these integrals using the global representation described above with self-consistent interpolation of the temperature field from the finite element approximation (15). In addition, several measures of the model problems presented here indicate that there was negligible loss of accuracy using this global approach. The details of these integral evaluations are presented in Appendix C.

Swartz–Wendroff approximation

It is possible to make an approximation to the residual equations which significantly reduces computational effort for systems of equivalent optical thickness where the geometry does not change and the finite element mesh is fixed in position. The general idea, originally employed by Swartz and Wendroff[55], is that one can simplify a problem considerably, often with negligible loss of accuracy, by applying mathematical operations only to the unknown coefficients of an expansion. In the context of our finite element methodology, this idea can be used to approximate the T^4 functionality in all radiation terms, so that:

$$T^4(r,z) = \left(\sum_{i=1}^{N_T} T^{(i)} \Phi^i(r,z) \right)^4 \approx \sum_{i=1}^{N_T} T^{(i)4} \Phi^i(r,z) \tag{34}$$

Since Lagrangian finite element basis functions are defined to be unity at one node of the mesh and zero at the rest, this relation is exact at each node. This approximation has been independently employed in the analysis of radiation heat transfer among surfaces in an enclosure containing a non-participating medium by Dupret *et al.*[43]; however, it has not previously been applied to the problem of radiative transport in a participating medium.

This technique is similar in spirit to zonal methods[56,57] and exchange-factor methods[35] which approximate radiative energy exchange among constant-temperature volume elements. These methods allow for the independent calculation of geometrical factors, thus speeding repeated heat transfer calculations; however, their utility is limited by the assumption of isothermal zones and the general difficulty of implementation with finite-difference or finite-element meshes[4,35]. The Swartz–Wendroff approximation employed here does not suffer from these limitations, since it can be consistently applied to any representation of the temperature field.

Using this approximation, we simplify the residual equations (17) and (21) to:

$$\int_{\partial D_f} \Phi^i(r,z)[\mathbf{q}_b \cdot \mathbf{n}_b]\, dS + \frac{4N}{\tau} \sum_{j=1}^{N_T} T^{(j)} \left[\int_D \nabla \Phi^i(r,z) \cdot \nabla \Phi^j(r,z)\, dV \right] - \sum_{j=1}^{N_T} T^{(j)4} A_{ij} - \sum_{j=1}^{N_{Tb}} T_b^{(j)4} B_{ij} - \sum_{j=1}^{Nq} q^{(j)} C_{ij} - \sum_{j=1}^{N_T} T^{(j)} E_{ij} - F_i(\mathbf{q}_b \mid \partial D_f) - K_i(T_b \mid \partial D_d) = 0 \tag{35}$$

and,

$$\sum_{j=1}^{Nq} q^{(j)} \left[\int_{\partial D_d} \Gamma^i \Gamma^j\, dS \right] - \int_{\partial D_d} \varepsilon T_b^4 \Gamma^i\, dS + \sum_{j=1}^{N_T} T^{(j)4} A_{ij}^* + \sum_{j=1}^{N_{Tb}} T_b^{(j)4} B_{ij}^* + \sum_{j=1}^{Nq} q^{(j)} C_{ij}^* + \sum_{j=1}^{N_T} T^{(j)} E_{ij}^* + F_i^*(\mathbf{q}_b \mid \partial D_f) + K_i^*(T_b \mid \partial D_d) = 0 \tag{36}$$

respectively.

The matrices (**A**, **A***, **B**, **B***, **C**, **C***), and the vectors (**F**, **F***, **K**, **K***), represent geometric factors weighted by a given optical thickness, τ, that are independent of the temperature field and can therefore be evaluated once and then stored. The expressions defining these matrices and vectors are presented in Appendix D. It should be stressed, however, that these expressions are

mesh-dependent, so that any technique which results in a different mesh, such as the front-tracking methods mentioned earlier, cannot fully exploit these computational savings.

An additional advantage of employing the Swartz–Wendroff formulation is considerable simplification of the Jacobian matrix entries. Closed-form expressions for all entries are easily defined as,

$$J_{ij}=\frac{\partial R_i}{\partial x_j}=\begin{cases}-C_{il} & x_j=q^{(l)}\\ \left[\dfrac{4N}{\tau}\displaystyle\int_D \nabla\Phi^i(r,z)\cdot\nabla\Phi^l(r,z)\,\mathrm{d}V-4T^{(l)^3}A_{il}-E_{il}\right] & x_j=T^{(l)}\\ \left[\dfrac{4N}{\tau}\displaystyle\int_D \nabla\Phi^i(r,z)\cdot\nabla\Phi^l(r,z)\,\mathrm{d}V-4T^{(l)^3}A_{il}-4T_b^{(m)^3}B_{im}-E_{il}\right] & x_j=T^{(l)}=T_b^{(m)}\end{cases} \tag{37}$$

when R_i corresponds to (35), and

$$J_{ij}=\frac{\partial R_i}{\partial x_j}=\begin{cases}\displaystyle\int_{\partial D_a}\Gamma^i\Gamma^k\,\mathrm{d}S+C^*_{ik} & x_j=q^{(k)}\\ 4T^{(k)^3}A^*_{ik}+E^*_{ik} & x_j=T^{(k)}\\ 4T^{(k)^3}A^*_{ik}+4T_b^{(l)^3}B^*_{il}+E^*_{ik} & x_j=T^{(k)}=T_b^{(l)}\end{cases} \tag{38}$$

when R_i corresponds to (36).

RESULTS

We present results from the two model problems in the following sections. The first involves a simple finite cylinder which was chosen to benchmark our method against other published results. The second example, a quasi-steady-state model for Bridgman growth of semitransparent crystals, demonstrates the versatility of our method for more complicated geometries and boundary conditions.

Participating medium contained by a right circular cylinder

For this problem, the arbitrarily shaped top and bottom of the general geometry were chosen to be flat surfaces so that the system becomes a finite right circular cylinder. A uniform heat generation term is added to the energy balance so that the temperature residual equation (17) becomes,

$$\int_{\partial D_f}\Phi^i(r,z)(\mathbf{q}_b\cdot\mathbf{n}_b)\,\mathrm{d}S-\int_0^{\Lambda^{-1}}\int_0^1\nabla\Phi^i(r,z)\cdot\left(-\frac{4N}{\tau}\nabla T+\mathbf{q}_R\right)r\,\mathrm{d}r\,\mathrm{d}z - Q\int_0^{\Lambda^{-1}}\int_0^1\Phi^i(r,z)r\,\mathrm{d}r\,\mathrm{d}z=0 \tag{39}$$

where $\Lambda\equiv R/L$ is the aspect ratio of the cylinder (R is the radius of the cylinder and L is its height) and Q is a uniform volumetric heating term.

The simple shapes of the top and bottom boundary allow for an explicit formulation of the problem without employing the transformation $\theta\rightarrow y$ described earlier and in Appendix B. In all calculations, unless stated otherwise, a mesh measuring sixteen biquadratic quadrilateral elements in the axial direction and ten elements in the radial direction was used, resulting in a total of $N_T=693$ temperature unknowns. The longitude α was divided into six equal segments, and a three-point quadrature rule was applied in each segment. Within each of the three regions $0\leqslant\theta\leqslant\theta_2$, $\theta_2<\theta<\theta_1$, and $\theta_1\leqslant\theta\leqslant\pi$) in the meridional planes (constant α), the colatitude

θ was divided into six equal segments, and a three point quadrature rule was applied in each segment. The path integrals were discretized using a single segment with five Gauss points. These discretizations of the finite element mesh and radiation integration quadrature yielded temperature fields which were numerically convergent.

The Swartz–Wendroff approximation was employed in the solution of this problem. Typical computation times of 100–250 CPU seconds were needed for the Swartz–Wendroff geometric factors. These factors needed to be calculated just once for a given discretization. Each Newton–Raphson iteration required approximately 10–15 CPU seconds. All times reported here were obtained on the Cray-2 at the Minnesota Supercomputer Center. Generally, 5 or 6 iterations were needed to converge with a criterion of $\|\delta^{(k)}\|_2 < 10^{-7}$.

Several cases of this model problem are examined below. First, the aspect ratio of the cylinder, Λ, is varied to approximate an infinite parallel plate geometry ($\Lambda \to \infty$) and an infinite cylinder ($\Lambda \to 0$), and our results are compared to prior literature values. Finally, a two-dimensional geometry with simple boundary conditions is tested against results in the literature, and new results for the same geometry with more complicated boundary conditions are generated to demonstrate the versatility of our method.

Infinite parallel plates: $\Lambda \to \infty$. For this case, the aspect ratio of the cylinder was set to $\Lambda = 100$, approximating a pair of infinite parallel plates. Dirichlet conditions were enforced along all exterior surfaces; the dimensionless temperature of the lower surface was set to $T_{b1} = 0.5$ and the upper surface temperature was set to $T_{b2} = 1$. To ensure that the problem is well-posed, the edge temperature T_{b3} was set to a linear profile connecting both the upper and lower surface temperatures. The heat generation term in (39) was set to zero ($Q = 0$). Centreline temperature profiles are shown as lines in *Figure 6* for various values of the wall emissivity for the case of $N = 0.01$ and $\tau^* \equiv \tau/\Lambda = 1$. The temperature profiles clearly show the non-linear effects caused by radiative transport. The discrete points plotted in *Figure 6* are obtained from the work of Viskanta and Grosh[8], who applied the method of successive approximations to the problem of transport between flat plates. The agreement between our results and those obtained by Viskanta and Grosh[8] is excellent for $\varepsilon_i = 1.0$ and $\varepsilon_i = 0.5$. However, our temperature profiles for $\varepsilon_i = 0.1$ differ slightly from the results of Viskanta and Grosh[8].

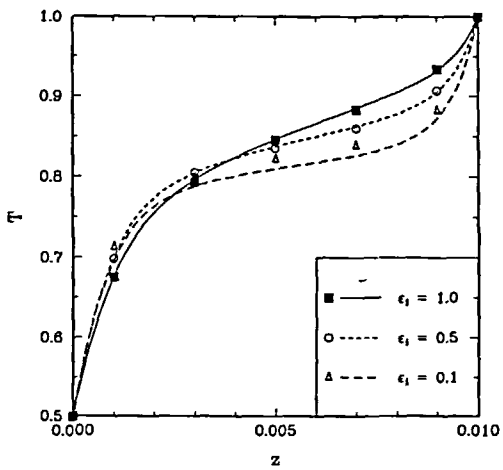

Figure 6 Centreline ($r = 0$), axial temperature profiles in a finite cylinder for $\Lambda = 100$, $N = 0.01$, $\tau^* = 1.0$ and $Q = 0.0$ (lines), together with the temperature distribution between flat plates due to Viskanta and Grosh[8] (discrete points)

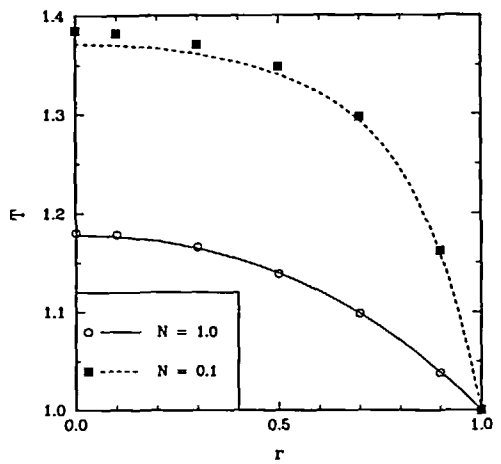

Figure 7 Mid-height ($z = 50$), radial temperature profiles in a finite cylinder for $\Lambda = 0.01$, $\tau = 1.0$, $\varepsilon_i = 1.0$ and $Q = 4.0$ (lines), together with the radial temperature distribution in an infinite cylinder due to Yücel and Williams[23] (discrete points)

Table 1 Total heat fluxes in the limit of flat plates ($\Lambda \to \infty$)

	Total axial flux			
Parameter values	This study $(-\mathbf{q}_T(0,0)\cdot\mathbf{e}_z)$	Viskanta and Grosh[8]	Pandey[24]	Crosbie and Viskanta[9]
$N = 0.01$ $\tau^* = 1.0$ $\varepsilon_i = 1.0$	0.5676	0.596	0.546	0.5675
$N = 0.01$ $\tau^* = 1.0$ $\varepsilon_i = 0.5$	0.3272	0.338	—	—
$N = 0.01$ $\tau^* = 1.0$ $\varepsilon_i = 0.1$	0.1566	0.156	—	—
$N = 0.01$ $\tau^* = 0.1$ $\varepsilon_i = 1.0$	1.0798	1.074	1.090	1.0799
$N = 0.1$ $\tau^* = 1.0$ $\varepsilon_i = 1.0$	0.7694	0.798	0.736	0.7694
$N = 0.1$ $\tau^* = 0.1$ $\varepsilon_i = 1.0$	2.8799	2.880	2.885	2.8799

Values of the centreline axial total heat flux for different values of ε_i, N and τ^*, are tabulated in *Table 1* together with fluxes reported in Ref. 8, as well as those reported by Crosbie and Viskanta[9] who also studied transport between flat plates. Also included in this Table are fluxes calculated by Pandey[24] for the case of heat transport between infinite concentric cylinders at the limit of equal inner and outer radii. Our flux values are in good agreement with all three studies.

Infinite cylinder: $\Lambda \to 0$. The limit of an infinite cylinder was approximated by setting $\Lambda = 0.01$. In addition, values of $Q = 4.0$ and $\tau = 1.0$ were used with Dirichlet boundary conditions of $T_b = 1.0$ on all three surfaces of the cylinder. Mid-height ($z = 50$) radial temperature profiles are plotted in *Figure 7* for two different values of the conduction-to-radiation parameter (N). The discrete points represent results obtained by Yücel and Williams[23] for an infinite cylinder using a combined discrete ordinates/finite differences method. The agreement between our results and those presented by Yücel and Williams is excellent[23] for $N = 1.0$ and good for $N = 0.1$.

Finite right circular cylinder. Our method was also tested against previous two-dimensional results obtained by Yücel and Williams[23], whose method combines discrete ordinates and finite differences. The aspect ratio of the cylinder was set at $\Lambda = 0.5$, the heat generation term was taken to be $Q = 4\tau$, and all boundaries were held at a uniform temperature of $T_b = 1.0$. Extensive tests were conducted for various values of τ, N, and ε_i. Solid lines in *Figure 8* show mid-height (unless stated otherwise) radial temperature profiles from this study, while the discrete points are from Reference 23.

The radial radiative flux, $\mathbf{q}_R\cdot\mathbf{e}_r$, and the radial total flux, $\mathbf{q}_T\cdot\mathbf{e}_r$, along the side wall are plotted as functions of z in *Figures 9* and *10*, respectively. The total flux was calculated using the consistent Galerkin FEM post-processing technique suggested by Gresho *et al.*[59], and the nodal values were spline fit in *Figure 10*. Agreement between our results and those of Yücel and Williams is excellent in most cases, though there are some discrepancies in the radiative flux

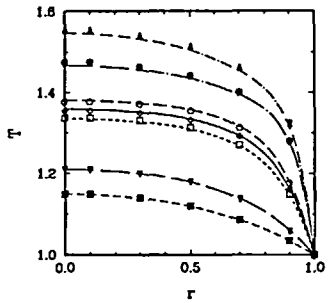

Figure 8 Radial temperature profiles in a finite cylinder, where $\Lambda = 0.5$ and $Q = 4\tau$, for different parameter values. Lines are a result of this work and discrete points are due to Reference 23. (a) $N = 1.0$, $\varepsilon_i = 1.0$, $\tau = 1.0$, and $z = 1.0$ (■); (b) $N = 0.1$, $\varepsilon_i = 1.0$, $\tau = 1.0$, and $z = 1.0$ (□); (c) $N = 0.1$, $\varepsilon_i = 0.7$, $\tau = 1.0$, and $z = 1.0$ (◇); (d) $N = 0.1$, $\varepsilon_i = 0.5$, $\tau = 1.0$, and $z = 1.0$ (○); (e) $N = 0.1$, $\varepsilon_i = 1.0$, $\tau = 0.5$, and $z = 1.0$ (▽); (f) $N = 0.1$, $\varepsilon_i = 1.0$, $\tau = 2.0$, and $z = 1.0$ (△); (g) $N = 0.1$, $\varepsilon_i = 1.0$, $\tau = 2.0$, and $z = 1.7$ (●)

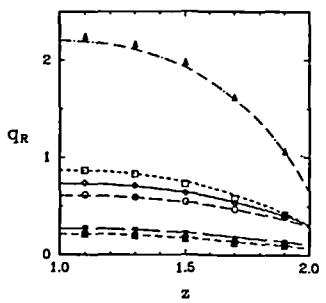

Figure 9 Radiative heat flux along the top half of the side wall of the cylinder, where $\Lambda = 0.5$ and $Q = 4\tau$, for different parameter values. Lines are a result of this work and discrete points are due to Reference 23. (a) $N = 1.0$, $\varepsilon_i = 1.0$, $\tau = 1.0$, and $z = 1.0$ (■); (b) $N = 0.1$, $\varepsilon_i = 1.0$, $\tau = 1.0$, and $z = 1.0$ (□); (c) $N = 0.1$, $\varepsilon_i = 0.7$, $\tau = 1.0$, and $z = 1.0$ (◇); (d) $N = 0.1$, $\varepsilon_i = 0.5$, $\tau = 1.0$, and $z = 1.0$ (○); (e) $N = 0.1$, $\varepsilon_i = 1.0$, $\tau = 0.5$, and $z = 1.0$ (▽); (f) $N = 0.1$, $\varepsilon_i = 1.0$, $\tau = 2.0$, and $z = 1.0$ (△)

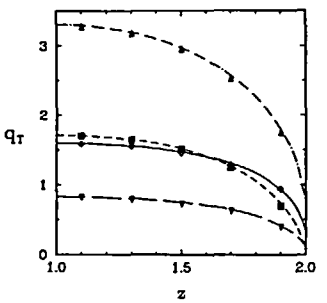

Figure 10 Total heat flux along the top half of the side wall of the cylinder, where $\Lambda = 0.5$ and $Q = 4\tau$, for different parameter values. Lines are a result of this work and discrete points are due to Reference 23. (a) $N = 1.0$, $\varepsilon_i = 1.0$, $\tau = 1.0$, and $z = 1.0$ (■); (b) $N = 0.1$, $\varepsilon_i = 0.7$, $\tau = 1.0$, and $z = 1.0$ (◇); (c) $N = 0.1$, $\varepsilon_i = 1.0$, $\tau = 0.5$, and $z = 1.0$ (▽); (d) $N = 0.1$, $\varepsilon_i = 1.0$, $\tau = 2.0$, and $z = 1.0$ (△)

values close to the top (or bottom) of the cylinder in some of the cases, as well as an overall small discrepancy in the results corresponding to the case of $N = 0.1$, $\tau = 2.0$ and $\varepsilon_i = 1.0$.

Finally, we have made some calculations designed to show the versatility of this method in handling mixed boundary conditions and extreme parameter values (e.g. $\tau \ll 1$ and $\tau \gg 1$). In these calculations, the aspect ratio of the cylinder was set at $\Lambda = 1.0$, the heat generation term was discarded ($Q = 0$), and the wall emissivity was assumed to have a uniform value of $\varepsilon_i = 0.5$. The boundary conditions were set as follows. Along the bottom surface, a no-flux boundary condition was specified,

$$\mathbf{q}_T \cdot (-\mathbf{e}_z)|_{(r,z=0)} = (\mathbf{q}_R + \mathbf{q}_c) \cdot (-\mathbf{e}_z)|_{(r,z=0)} = 0 \tag{40}$$

a constant temperature was set along the top surface using a Dirichlet condition

$$T(r, z = 1.0) = 1 \tag{41}$$

and a position-dependent temperature was applied at the wall of the cylinder,

$$T(r = 1, z) = \tfrac{1}{4}\{3 + \cos[(1 - z)\pi]\} \tag{42}$$

For this case, the discretization was further refined to a mesh of 14 × 14 uniform biquadratic elements. In addition, ray length integrals were discretized using a single nine quadrature point segment; however, the discretization of the solid angle integrals (θ, α) remained the same as in the earlier examples. The temperature field is well-resolved for all cases.

Temperature contours for various values of N and τ are shown in *Figure 11*. For the case of a large conduction-to-radiation parameter, $N = 100$, the temperature field remains conduction dominated regardless of the value of τ. For these cases, the temperature contours enter the bottom surface perpendicularly, which is consistent with the conductive flux dominating the no-flux boundary condition (40).

For the lower values of the conduction-to-radiation parameter, $N = 0.01$, the temperature

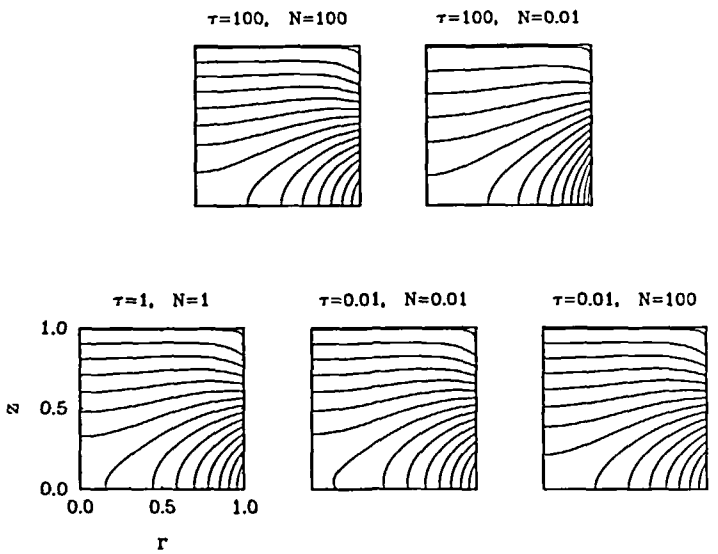

Figure 11 Temperature contours in the cylinder for different values of τ and N, where $\Lambda = 1.0$, $Q = 0$, and $\varepsilon_i = 0.5$. Boundary conditions are given in the text. In each plot, the first isotherm in the bottom right-hand corner corresponds to $T = 0.53309$, and neighbouring contours differ by $\Delta T = 0.03309$

field is strongly affected by radiative transport. In the case of the optically thick medium $\tau = 100$, the radiative interactions are confined to very short distances, and the radiative flux is governed by the Rosseland diffusion equation[1,58]

$$\tilde{q}_R \approx \frac{16n^2\sigma\tilde{T}^3}{3a}\nabla\tilde{T} \tag{43}$$

where the tilde denotes dimensional quantities. In this limit, the governing integro-differential equation behaves as the classical partial differential equation describing conduction heat transfer with an additional temperature-dependent term added to the thermal conductivity. Notice that the isotherm spacing in most of the domain is much larger than the cases of $N = 100$; here, the effective thermal conductivity is much larger due to the radiative contribution. In addition, a zero axial gradient is maintained at the bottom of the cylinder even though the transport is dominated by radiation. For the optically thin case of $\tau = 0.01$ (with $N = 0.01$), radiation is important and acts over the entire domain. A notable feature of this case is the significant departure of the isotherms along the bottom surface from the vertical. For this simulation, the radiative flux is significant at all surfaces; this effect, acting through (40), produces the slanting of the isotherms at the bottom surface.

The case of $\tau = 1$ and $N = 1$ is the most challenging and demonstrates that our method is viable for all values of radiation parameters. This result represents the situation where radiation and conduction heat transfer are everywhere important, and the temperature field is quite different from the conduction-dominated cases discussed above, especially along the bottom surface and centerline. There is a slight, but noticeable, deviation of the isotherms from the vertical as they meet the bottom surface, indicating the relative importance of the radiative flux component in the boundary condition.

Bridgman growth of a semitransparent crystal

Our final model problem demonstrates the utility of our method and, in fact, was the primary motivation for its development. A more complete set of results for a similar problem are given

elsewhere[36], and further enhancements of the model are discussed in a separate paper[3] . We consider the Bridgman growth of crystalline yttrium aluminium garnet (YAG), an important laser host material. Several experimental studies have speculated that internal radiative heat transfer strongly affects the crystal growth process for YAG[38,39].

The physical properties of our model system are listed in *Table 2*. Operating parameters and system geometry (taken from experimental literature) are listed in *Table 3*. Note that for this system the conduction-to-radiation parameter is $N = 0.13$, the optical thickness is $\tau = 0.65$, and the aspect ratio of the cylindrical ampoule is $\Lambda = 0.043$.

In the simulations presented here, 5 radial × 7 axial biquadratic elements were used in both the crystal and melt domains. The longitude α was divided into eight equal segments, and a three-point quadrature rule was applied in each segment. Within each of the two regions $\theta_2 < \theta < \theta_1$ and $\theta_1 \leqslant \theta \leqslant \pi$ (viewing the ampoule side wall and bottom surface, respectively), the colatitude θ was divided into eight equal segments, and a three point quadrature rule was applied in each segment. For the region which views the melt/crystal interface, $0 \leqslant \theta \leqslant \theta_2$, the transformation variable y was employed. The variable y was divided into eight equal segments, and a three point quadrature rule was applied in each segment. The path integrals were discretized

Table 2 Physical properties for the Bridgman crystal growth system

Description	Symbol	Value	Comments
Absorption coefficient	a	1.0 cm^{-1}	YAG crystal, estimated from Reference 61
Emissivity	ε_i	0.3	Molybdenum ampoule inner wall[1,62]
	ε_0	0.3	Molybdenum ampoule outer wall[1,62]
	ε_{ms}	0.3	estimated from properties of gadolinium gallium garnet (GGG)[63]
Heat of fusion	ΔH_f	455.4 J/g	estimated from properties of GGG[64]
Thermal conductivity	k_m	0.05 W/cm K	estimated from properties of GGG[64]
	k_s	0.1 W/cm K	YAG[65]
Refractive index	n	1.8	YAG crystal[66]
Density of solid	ρ_s	4.3 g/cm^3	YAG[67]
Melting point	$\tilde{T}_{mp}$	2243 K	YAG[68]

Table 3 Operating parameters for the Bridgman crystal growth system

Description	Symbol	Base case value	Comments
Furnace temperature gradient	G	80 K/cm	Symmetric about centre of adiabatic zone, estimated from Reference 69
Ambient heat transfer coefficient	h_{III}	3.5×10^{-3} W/cm^2 K	estimated[70]
	h_I, h_{II}	1.5×10^{-4} W/cm^2 K	estimated[70]
Ampoule length	L	15.0 cm	estimated[71,72]
Length of adiabatic zone	L_A	5.0 cm	—
Ampoule radius	R	0.65 cm	estimated[71,72]
Hot zone temperature	$\tilde{T}_h$	2443 K	—
Cold zone temperature	$\tilde{T}_c$	2043 K	—
Ampoule pull rate	V_p	3.6 mm/h	estimated[71,72]
Position of adiabatic zone centre	$\tilde{z}_A$	7.5 cm	Varied from 2.5 cm to 12.5 cm

using a single segment with five Gauss points. Convergence tests were performed using these discretizations; selected test-case temperature contours and interface shapes were found not to change in appearance upon further discretization. Typical CPU requirements on the Cray-2 supercomputer were approximately 7 min per iteration with 5–7 iterations needed for convergence using the same convergence criterion as before, $\|\delta^{(k)}\|_2 < 10^{-7}$. The relatively higher CPU times for this model are due to the finer discretizations employed and the inability to apply the Swartz–Wendroff approximation method.

The results shown here simulate stages of a growth run, in which the relative position of the adiabatic zone shifts along the ampoule. The temperature field and interface shape were recalculated at each new position of the ampoule within the furnace. As can be seen in *Figure 12*, the isotherms do not change much in shape or position relative to the interface.

There is a small increase in the centreline axial temperature gradient in the melt at the interface as the solidification process proceeds (see *Figure 13*), and a corresponding decrease of the gradient on the crystal side of the interface. Both of these trends diminish towards the end of the growth run. These effects are explained by the changing geometry of the crystalline phase and the changing position of the ampoule in the furnace as growth proceeds. The radiative flux through the crystal increases as the bottom of the ampoule moves progressively further into the cold zone and the lower portions of crystal and ampoule cool. This effect increases the overall axial heat flux through the system, which is matched by the increasing axial gradient in the melt. The increase in axial flux through the crystalline phase is due wholly to radiative transport; in fact, so much heat is transported by radiant energy that the axial conductive flux in the crystal actually decreases as growth proceeds, as indicated by the decrease in the crystal temperature gradient. These trends lessen as the growth progresses, since there is a continuing increase in the axial optical thickness which causes a radiative screening effect—the lower, cooler portions

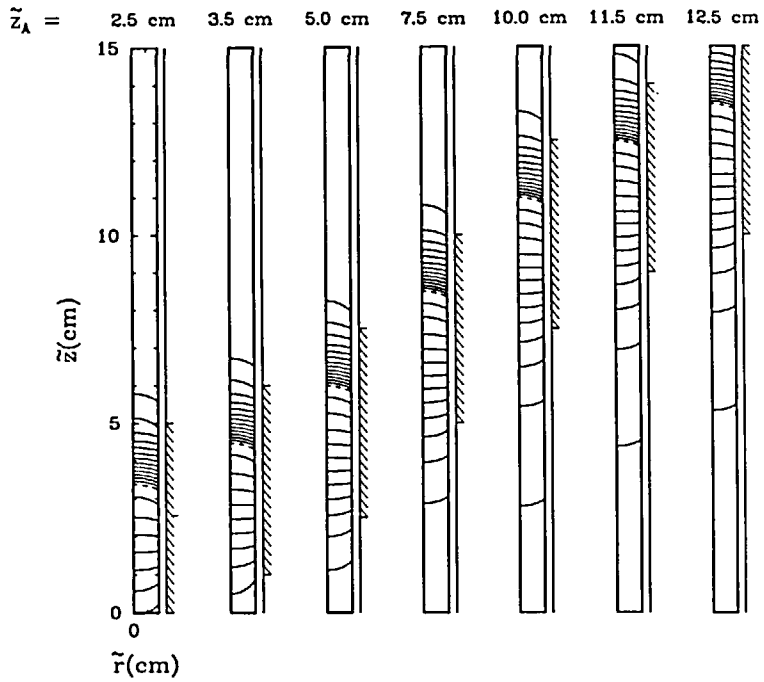

Figure 12 Temperature contours in solid and melt during simulated growth of a YAG crystal. The position of the melt/crystal interface position is indicated by a broken line, contour spacing is 15 K, and the position of the adiabatic zone is indicated by a shaded region adjacent to the ampoule side

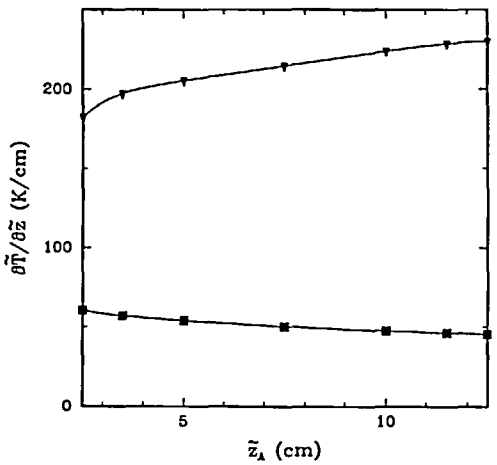

Figure 13 Axial, centreline ($r = 0$) temperature gradients at the interface in the melt (triangles) and the crystal (squares) during a simulated growth run of a YAG crystal

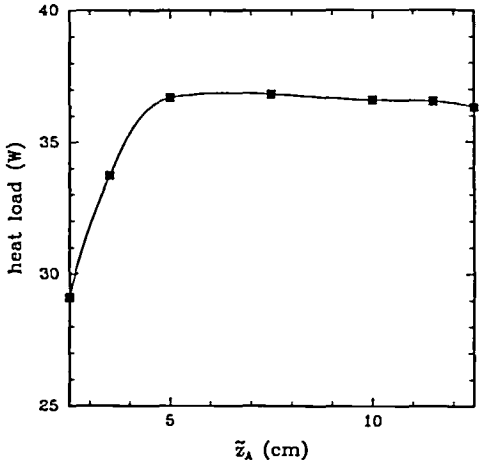

Figure 14 The heat load (defined in text) *versus* the position of the centre of the adiabatic zone ($\tilde{z}_A$)

of the crystal and ampoule become optically far enough from the interface that their effect on the overall heat transfer is eventually attenuated.

These effects were further investigated by examining the 'heat load' in *Figure 14*. The heat load is a measure of the total thermal energy flowing through the system and is calculated as the integrated positive heat flux (i.e. pointing inwards) over the ampoule. This quantity rises rapidly as growth initially proceeds and soon attains a nearly constant value for the rest of the run. This is in agreement with the above explanation of the results presented in *Figure 13*. The radiative screening effect is readily apparent by the leveling of the curve at $z_A \approx 5$ cm in *Figure 14*. The more dramatic change of the heat load compared to the axial temperature gradients as growth proceeds is due to the fact that the heat load is an integrated measure, taking into account the full geometry of the system, while the axial centreline gradients represent local, one-dimensional quantities.

Finally, melt/crystal interface shapes are shown in *Figure 15*. These shapes do not exhibit drastic changes in curvature during the growth, thus indicating that the heat transfer through the system is dominated by axial fluxes. This is expected for the small aspect ratio of this geometry (long, slender ampoule) which is nearly one-dimensional; however, when the crystal is grown in an ampoule whose thickness is not negligible, there is more radial curvature present in the interface with internal radiation acting than for the case of conduction heat transfer alone[37].

CONCLUSIONS

A robust Galerkin finite element method for the solution of combined radiative and conductive transport in axisymmetric geometries of any optical thickness has been developed. The accuracy of the method has been tested successfully against several benchmark solutions, and its versatility was demonstrated in a complicated free-boundary problem, with reasonable associated computational costs. Significant computational savings are possible by taking advantage of the Swartz–Wendroff approximation, which, for a fixed discretized geometry and optical thickness, allows geometric factors to be calculated once and used over again. This is very useful when repeating similar calculations on the same system.

One difficulty encountered here in solving the integro-differential equations describing

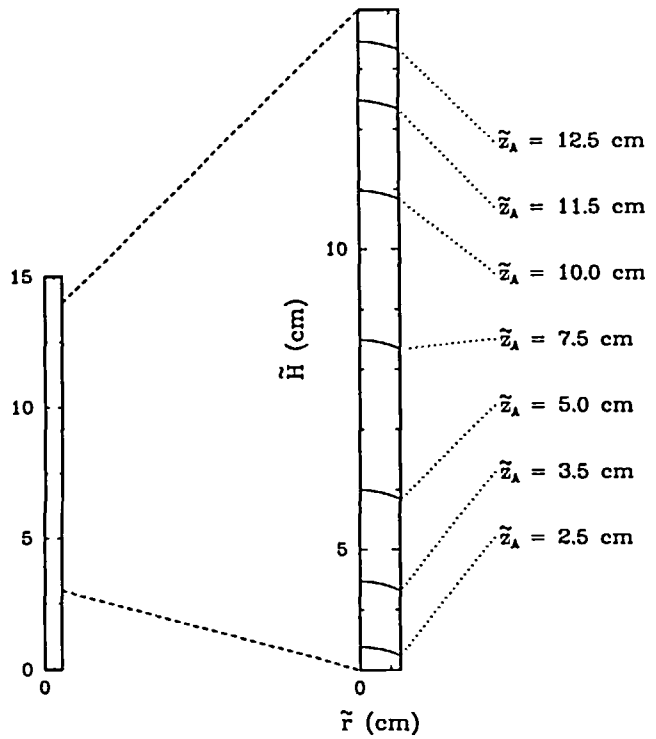

Figure 15 Interface shapes and positions for a simulated growth of a YAG crystal. For clarity, only the middle section of the ampoule is shown

combined mode, conduction–radiation heat transfer is that testing for convergence of the method is not nearly as straightforward as in more conventional heat transfer problems (i.e. those described by partial differential equations). Not only must one check for numerical convergence by refining the finite element mesh, one must also refine the quadrature (in three separate discretizations) for the radiation integrals. The effects of changing all four discretizations are mutually dependent. To ensure a numerically convergent solution, one must make sure that convergence is obtained in all four and is sustained upon further refinement of one or more of the discretizations. This feature, which is often overlooked by practitioners, is generic to any solution method applied to integro-differential equations.

There are several extensions to this method which are of interest. Since the main complexity of this method is associated with the evaluation of the three-dimensional, solid angle radiation integrals, extensions to a fully three-dimensional temperature field should be relatively straightforward to implement. However, the associated computational cost will increase substantially, since many more integral evaluations will be needed for a three-dimensional finite element mesh. Including most temperature-dependent properties in the analysis is straightforward, although potential difficulties arise in several situations. One complication, which arises from a temperature-dependent absorption coefficient (or dimensionless optical thickness, τ), is created by the need to relate the geometric path length l to the optical path length κ, which is the quantity which rigorously appears in the exponential terms of the integrated equation of transfer,

$$i'(\Omega) = i'(\Omega, 0)\exp[-\kappa(\Omega)] + \frac{1}{\pi}\int_0^l \tau(l')T^4(l')\exp[-(\kappa - \kappa')]\,\mathrm{d}l' \qquad (44)$$

For a non-uniform absorption coefficient,

$$\kappa(l) = \int_0^l \tau(l^\dagger)\, dl^\dagger \tag{45}$$

Including a temperature-dependent refractive index n in the analysis is very difficult, since ray paths would curve in space from this effect. Fortunately, n is usually a weak function both of temperature and of wavelength in semitransparent solids, see for example Reference 60. The incorporation of wavelength-dependent properties is straightforward; however, an extra integration (over wavelength) must be performed, creating a considerable increase in computational expense. Already, most of the effort involves evaluation of the radiative terms.

Including the effects of scattering should not, in principle, be difficult. For example, this can be achieved in many cases by considering a position-dependent source function to be determined by scattering relationships and expanded with a separate finite element basis set[32]. This particular extension is not important, however, for modelling the solidification of semitransparent crystals, since scattering is usually negligible in a large, pure crystal.

Application of this method to other research areas is of interest. These include the study of glass processing, optical fibre drawing techniques, and combustion systems, amongst others. Obviously, in some applications, one must be careful and take into account effects neglected here (e.g. scattering in combustion furnaces, see previous paragraph).

ACKNOWLEDGEMENTS

The authors are grateful to the Microgravity Sciences Program of the National Aeronautics and Space Administration, the Minnesota Supercomputer Institute, and the Army High Performance Computing Center for partial support of this research. J.J.D. also acknowledges support from the National Science Foundation PYI award program. S.B. was supported in part by the Graduate School of the University of Minnesota through a Doctoral Dissertation Fellowship. The authors also wish to express their appreciation to Prof. Haeok S. Lee of the University of Minnesota for her advice and encouragement early-on in this work.

Parts of this work were presented at the 1991 National Heat Transfer Conference, Minneapolis, MN, July 28–31.

REFERENCES

1 Siegel, R. and Howell, J. R. *Thermal Radiation Heat Transfer*, Second Edition, McGraw-Hill, New York (1981)
2 Howell, J. R. Thermal radiation in participating media: the past, the present, and some possible futures, *J. Heat Transfer*, **110**, 1220–1229 (1988)
3 Chan, S. H. Numerical methods for multidimensional radiative transfer analysis in participating media, *A. Rev. Num. Fluid Mech. Heat Transfer*, **1**, 305–350 (1987)
4 Viskanta, R. and Mengüç, M. P. Radiation heat transfer in combustion systems, *Progr. Energy Combust. Sci.*, **13**, 97–160 (1987)
5 Chandrasekhar, S. *Radiative Transfer*, Clarendon Press, Oxford (1950)
6 Kourganoff, V. *Basic Methods in Transfer Problems*, Clarendon Press, Oxford (1952)
7 Goody, R. M. *Atmospheric Radiation. Theoretical Basis*, Clarendon Press, Oxford, Vol. I (1964)
8 Viskanta, R. and Grosh, R. J. Effect of surface emissivity on heat transfer by simultaneous conduction and radiation, *Int. J. Heat Mass Transfer*, **5**, 729–734 (1962)
9 Crosbie, A. L. and Viskanta, R. Interaction of heat transfer by conduction and radiation in a nongray planar medium, *Wärme Sotffübertrag.*, **4**, 205–212 (1971)
10 Crosbie, A. L. and Dougherty, R. L. Two-dimensional radiative transfer in a cylindrical geometry with anisotropic scattering, *J. Quant. Spectrosc. Radiat. Transfer*, **25**, 551–569 (1981)
11 Perlmutter, M. and Howell, J. R. Radiant transfer through a gray gas between concentric cylinders using Monte Carlo, *J. Heat Transfer*, **86**, 169–179 (1964)
12 Kesten, A. S. Radiant heat flux distribution in a cylindrically-symmetric nonisothermal gas with temperature-dependent absorption coefficient, *J. Quant. Spectrosc. Radiat. Transfer*, **8**, 419–434 (1968)

13 Dua, S. S. and Cheng, P. Multi-dimensional radiative heat transfer in non-isothermal cylindrical media with non-isothermal bounding walls, *Int. J. Heat Mass Transfer*, **18**, 245–258 (1975)
14 Crosbie, A. L. and Farrell, J. B. Exact formulation of multiple scattering in a three-dimensional cylindrical geometry, *J. Quant. Spectrosc. Radiat. Transfer*, **31** (5), 397–416 (1984)
15 Lin, J. D. Exact expressions for radiative transfer in an arbitrary geometry exposed to radiation, *J. Quant. Spectrosc. Radiat. Transfer*, **37** (6), 591–601 (1987)
16 Thynell, S. T. The integral form of the equation of transfer in finite, two-dimensional, cylindrical media, *J. Quant. Spectrosc. Radiat. Transfer*, **42** (2), 117–136 (1989)
17 Thynell, S. T. Treatment of radiation heat transfer in absorbing, emitting, scattering, two-dimensional cylindrical media, *Num. Heat Transfer (A)*, **17**, 449–472 (1990)
18 Siegel, R. Transient radiative cooling of an absorbing and scattering cylinder—A separable solution, *J. Thermophys.*, **2** (2), 110–117 (1988)
19 Siegel, R. Transient radiative cooling of an absorbing and scattering cylinder, *J. Heat Transfer*, **111**, 199–203 (1989)
20 Kim, T. K. and Smith, T. F. Radiative and conductive transfer for a real gas in a cylindrical enclosure with gray walls, *Int. J. Heat Mass Transfer*, **28**, 2269–2277 (1985)
21 Al-Turki, A. M. and Smith, T. F. Radiative and convective transfer in a cylindrical enclosure for a gas/soot mixture, *J. Heat Transfer*, **109**, 259–261 (1987)
22 Tabanfar, S. and Modest, M. F. Combined radiation and convection in absorbing, emitting, nongray gas-particulate tube flow, *J. Heat Transfer*, **109**, 478–484 (1987)
23 Yücel, A. and Williams, M. L. Heat transfer by combined conduction and radiation in axisymmetric enclosures, *J. Thermophys.*, **1** (4), 301–306 (1987)
24 Pandey, D. K. Combined conduction and radiation heat transfer in concentric cylindrical media, *J. Thermophys.*, **3** (1), 75–82 (1989)
25 Harris, J. A. Solution of the conduction/radiation problem with linear-anisotropic scattering in an annular medium by the spherical harmonics method, *J. Heat Transfer*, **111**, 194–197 (1989)
26 Lewis, E. E. and Miller, Jr., W. F. *Computational Methods of Neutron Transport*, Wiley, New York (1984)
27 Wu, S. T., Ferguson, R. E. and Altgilbers, L. L. Application of finite-element techniques to the interaction of conduction and radiation in a participating medium, in *Heat Transfer and Thermal Control* (Ed. A. L. Crosbie), AIAA, New York, *Progr. Astronaut. Aeronaut.*, **78**, 61–91 (1980)
28 Fernandes, R., Francis, J. and Reddy, J. N. A finite-element approach to combined conductive and radiative heat transfer in a planar medium, in *Heat Transfer and Thermal Control* (Ed. A. L. Crosbie), AIAA, New York, pp. 92–109 (1980)
29 Fernandes, R. L. and Francis, J. E. Combined radiative and conductive heat transfer in a planar medium with a flux boundary condition using finite elements, *AIAA Paper No. AIAA-82-0910* (1982)
30 Razzaque, M. M., Klein, D. E. and Howell, J. R. Finite element solution of radiative heat transfer in a two-dimensional rectangular enclosure with gray participating medium, *J. Heat Transfer*, **105**, 933–934 (1983)
31 Razzaque, M. M., Howell, J. R. and Klein, D. E. Coupled radiative and conductive heat transfer in a two-dimensional rectangular enclosure with gray participating media using finite elements. *J. Heat Transfer*, **106**, 613–619 (1984)
32 Chung, T. J. and Kim, J. Y. Two-dimensional, combined-mode heat transfer by conduction, convection, and radiation in emitting, absorbing, and scattering media-solution by finite elements, *J. Heat Transfer*, **106**, 448–452 (1984)
33 Dombrovskii, L. A. and Barkova, L. G. Solving the two-dimensional problem of thermal-radiation transfer in an anisotropically scattering medium using the finite element method, *Teplofiz. Vys. Temp.*, **24** (4), 762–769 (1986)
34 Kraus, H. G. Hybrid finite element–Monte Carlo method for coupled conduction and gas radiation enclosure heat transport, *Int. J. Num. Meth. Eng.*, **26**, 361–378 (1988)
35 Saltiel, C. and Naraghi, M. H. N. Analysis of radiative heat transfer in participating media using arbitrary nodal distribution, *Num. Heat Transfer (B)*, **17**, 227–243 (1990)
36 Brandon, S. and Derby, J. J. Internal radiative transport in the vertical Bridgman growth of semitransparent crystals, *J. Crystal Growth*, **110**, 481–500 (1991)
37 Brandon, S. and Derby, J. J. Heat transfer in vertical Bridgman growth of oxides: Effects of conduction, convection, and internal radiation, *J. Crystal Growth*, **121**, 473–494 (1992)
38 Butaeva, T. I., Gevorkyan, A. V., Kuzanyan, A. S. and Petrosyan, A. G. Interface shape of aluminium garnets growth from melts, *Dokl Akad. Nauk. Arm. SSR*, **84** (1), 38–40 (1987)
39 Kvapil, Ji., Kvapil, Jo., Manek, B., Perner, B., Autrata, B. and Schauer, P. Czochralski growth of YAG:Ce in a reducing protective atmosphere, *J. Crystal Growth.*, **52**, 542–545 (1981)
40 Brown, R. A. Theory of transport processes in single crystal growth from the melt, *AIChE J.*, **34**, 881–911 (1988)
41 Derby, J. J., Atherton, L. J. and Gresho, P. M. An integrated process model for the growth of oxide crystals by the Czochralski method, *J. Crystal Growth*, **97**, 792–826 (1989)
42 Crochet, M. J., Dupret, F., Ryckmans, Y., Geyling, F. T. and Monberg, E. M. Numerical simulation of crystal growth in a vertical Bridgman furnace, *J. Crystal Growth*, **97**, 173–185 (1989)
43 Dupret, F., Nicodème, P., Ryckmans, Y., Wouters, P. and Crochet, M. J. Global modelling of heat transfer in crystal growth furnaces, *Int. J. Heat Mass Transfer*, **33**, 1849–1871 (1990)
44 Thomas, P. D., Derby, J. J., Atherton, L. J. and Brown, R. A. Dynamics of liquid encapsulated Czochralski growth of gallium arsenide: comparing model with experiment, *J. Crystal Growth*, **96**, 135–152 (1989)

45 O'Hara, S., Tarshis, L. A. and Viskanta, R. Stability of the solid-liquid interface of semi-transparent materials, *J. Crystal Growth*, **3/4**, 583–593 (1968)
46 Abrams, M. and Viskanta, R. The effects of radiative heat transfer upon the melting and solidification of semitransparent crystals, *J. Heat Transfer*, **96**, 184–190 (1974)
47 Antonov, P. I., Bakholdin, S. I., Tropp, E. A. and Yuferev, V. S. An experimental and theoretical study of temperature distribution in sapphire crystals grown from the melt by Stepanov's method, *J. Crystal Growth*, **50**, 62–68 (1980)
48 Yuferev, V. S. and Vasil'ev, M. G. Heat transfer in shaped thin-walled semi-transparent crystals pulled from the melt, *J. Crystal Growth*, **82**, 31–38 (1987)
49 Kim, K. S. and Yimer, B. Thermal radiation heat transfer effects on solidification of finite concentric cylindrical medium-enthalpy model and P-1 approximation, *Num. Heat Transfer*, **14**, 483–498 (1988)
50 Matsushima, H. and Viskanta, R. Effects of internal radiative transfer on natural convection and heat transfer in a vertical crystal growth configuration, *Int. J. Heat Mass Transfer*, **33**, 1957–1968 (1990)
51 Salinger, A. G., Brandon, S., Aris, R. and Derby, J. J. Buoyancy-driven flows of a radiatively-participating fluid in a vertical cylinder heated from below, *Proc. R. Soc.*, submitted (1992)
52 Gebhart, B. *Heat Transfer*, McGraw-Hill, New York, p. 133 (1971)
53 Ettouney, H. M. and Brown, R. A. Finite element methods for steady solidification problems, *J. Comp. Phys.*, **49**, 118–150 (1983)
54 Strang, G. and Fix, G. J. *An Analysis of the Finite Element Method*, Prentice-Hall, Englewood Cliffs, NJ (1973)
55 Swartz, B. and Wendroff, B. Generalized finite-difference schemes, *Math. Comp.*, **23**, 37–49 (1969)
56 Hottel, H. C. and E. S. Cohen, Radiant heat exchange in a gas-filled enclosure: allowance for nonuniformity of gas temperature, *AIChE J.*, **4**, 3–14 (1958)
57 Howell, J. R. Radiative transfer in multidimensional geometries, *ASME 83-HT-32* (1983)
58 Rosseland, S. *Theoretical Astrophysics; Atomic Theory and the Analysis of Stellar Atmospheres and Envelopes*, Clarendon Press, Oxford (1936)
59 Gresho, P., Lee, R., Sani, R. L., Maslanik, M. K. and Eaton, B. E. The consistent Galerkin FEM for computing derived boundary quantities in thermal and/or fluids problems, *Int. J. Num. Meth. Fluids*, **7**, 371 (1987)
60 Zharikov, E. V., Privis, Yu. S., Studenikin, P. A., Chikov, V. A., Shigorin, V. D. and Shcherbakov, I. A. Temperaturewise measurements of refractive indices of rare-earth garnets, *Sov. Phys. Crystallogr.*, **34** (5), 712–714 (1989)
61 Prikhod'ko, L. V. and Bagdasarov, Kh. S. Infrared absorption in yttrium–aluminum garnet crystals at high temperatures, *Krystallografiya*, **16** (4), 826–827 (1971)
62 *CRC Handbook of Chemistry and Physics*, 59th edn. (Ed. R. C. Weast and M. J. Astle), CRC Press, Florida (1978–1979)
63 Andrianova, V. G., Dozhidikov, V. S., Obukhov, O. Yu., Petrov, V. A., Reznik, V. Yu. and Sevrynkov, O. N. Optical properties of gadolinium–gallium garnet, *Trplofiz. Vys. Temp.*, **21** (4), 680–687 (1983)
64 Thermal and optical properties of GGG, *Report No. IBM PO N5730861 STH59*, Lockheed Missiles and Space Company, Palo Alto, CA
65 Slack, G. A. and Oliver, D. W. Thermal conductivity of garnets and phonon scattering by rare-earth ions, *Phys. Rev.* (*B*), **4** (2), 592–609 (1971)
66 Arutunyan, E. A. and Galoyan, S. Kh. Determination of refractive index profile in optical waveguides formed by ion implantation, *Optics Commun.*, **56** (6), 399–402 (1986)
67 Klein, P. H. and Croft, W. J. Thermal conductivity diffusivity and expansion of Y_2O_3, $Y_3Al_5O_{12}$, and LaF_3 in the range 77–300 K, *J. Appl. Phys.*, **38**, 1603 (1967)
68 Cockayne, B. The melt growth of oxide and related single crystals, *J. Crystal Growth*, **42**, 413–426 (1977)
69 Petrosyan, A. G. and Bagdasarov, Kh. S. Faceting in Stockbarger grown garnets, *J. Crystal Growth*, **34**, 110–112 (1976)
70 Welty, J. R., Wicks, C. E. and Wilson, R. E. *Fundamentals of Momentum, Heat, and Mass Transfer*, 3rd edn., John Wiley, New York (1984)
71 Peshev, P., Petrov, V. and Manilov, N. Growth and spectral characteristics of $Y_3Al_5O_{12}:Ti^{3+}$ single crystals, *Mat. Res. Bull.*, **23**, 1193–1198 (1988)
72 Peshev, P., Delineshev, S., Petrov, V., Manilov, N., Yankov, P. and Bachvarov, I. Bridgman–Stockbarger growth and spectral characteristics of $Al_2O_3:Ti^{3+}$ single crystals, *Cryst. Res. Technol.*, **23**, 641–645 (1988)
73 Dhatt, G. and Touzot, G. *The Finite Element Method Displayed*, John Wiley, New York (1984)

APPENDIX A

Net radiative flux at the system boundaries

The net radiative flux into the system at its boundaries, described in general terms by (19), is detailed below. The solid angle integral in this equation is similar to the one given in (29), except that the point of interest is on one of the boundaries, therefore the integral is only

performed over a hemisphere. The detailed form of (19) is given by the following expressions. Along the bottom boundary of the domain, we have

$$
\begin{aligned}
&\mathbf{q}_R\cdot(-\mathbf{n}_{b1})\\
&\quad=\varepsilon_{i1}\Bigg\{T_{b1}^4-\frac{2}{\pi}\int_0^{\pi}\Bigg\{\int_{\theta_1(x)}^{\theta_1'(x)}\left[T_{b1^*}^4-\frac{1-\varepsilon_{i1^*}}{\varepsilon_{i1^*}}\mathbf{q}_R\cdot(-\mathbf{n}_{b1^*})\right]\exp(-\tau l_1)\cos(\psi_{11})\sin(\theta)\,\mathrm{d}\theta\\
&\qquad+\int_0^{\theta_2(x)}\left[T_{b2^*}^4-\frac{1-\varepsilon_{i2^*}}{\varepsilon_{i2^*}}\mathbf{q}_R\cdot(-\mathbf{n}_{b2^*})\right]\exp(-\tau l_2)\cos(\psi_{12})\sin(\theta)\,\mathrm{d}\theta\\
&\qquad+\int_{\theta_2(x)}^{\theta_1(x)}\left[T_{b3^*}^4-\frac{1-\varepsilon_{i3}^*}{\varepsilon_{i3}^*}\mathbf{q}_R\cdot(-\mathbf{e}_r)|_{b3^*}\right]\exp(-\tau l_3)\cos(\psi_{13})\sin(\theta)\,\mathrm{d}\theta\\
&\qquad+\tau\Bigg[\int_{\theta_1(x)}^{\theta_1'(x)}\int_0^{l_1}T^4(l_1^{\dagger})\exp[-\tau(l_1-l_1^{\dagger})\,\mathrm{d}l_1^{\dagger}\cos(\psi_{11})\sin(\theta)\,\mathrm{d}\theta\\
&\qquad+\int_0^{\theta_2(x)}\int_0^{l_2}T^4(l_2^{\dagger})\exp[-\tau(l_2-l_2^{\dagger})]\,\mathrm{d}l_2^{\dagger}\cos(\psi_{12})\sin(\theta)\,\mathrm{d}\theta\\
&\qquad+\int_{\theta_2^{(x)}}^{\theta_1(x)}\int_0^{l_3}T^4(l_3^{\dagger})\exp[-\tau(l_3-l_3^{\dagger})]\,\mathrm{d}l_3^{\dagger}\cos(\psi_{13})\sin(\theta)\,\mathrm{d}\theta\Bigg]\Bigg\}\,\mathrm{d}\alpha\Bigg\}
\end{aligned}
\tag{46}
$$

The flux incoming from the top boundary is given by:

$$
\begin{aligned}
&\mathbf{q}_R\cdot(-\mathbf{n}_{b2})\\
&\quad=\varepsilon_{i2}\Bigg\{T_{b2}^4-\frac{2}{\pi}\int_0^{\pi}\Bigg\{\int_{\theta_1(x)}^{\pi}\left[T_{b1^*}^4-\frac{1-\varepsilon_{i1^*}}{\varepsilon_{i1^*}}\mathbf{q}_R\cdot(-\mathbf{n}_{b1^*})\right]\exp(-\tau l_1)\cos(\psi_{21})\sin(\theta)\,\mathrm{d}\theta\\
&\qquad+\int_{\theta_2'(x)}^{\theta_2(x)}\left[T_{b2^*}^4-\frac{1-\varepsilon_{i2^*}}{\varepsilon_{b2^*}}\mathbf{q}_R\cdot(-\mathbf{n}_{b2^*})\right]\exp(-\tau l_2)\cos(\psi_{22})\sin(\theta)\,\mathrm{d}\theta\\
&\qquad+\int_{\theta_2(x)}^{\theta_1(x)}\left[T_{b3^*}^4-\frac{1-\varepsilon_{i3^*}}{\varepsilon_{i3^*}}\mathbf{q}_R\cdot(-\mathbf{e}_r)|_{b3^*}\right]\exp(-\tau l_3)\cos(\psi_{23})\sin(\theta)\,\mathrm{d}\theta\\
&\qquad+\tau\Bigg[\int_{\theta_1(x)}^{\pi}\int_0^{l_1}T^4(l_1^{\dagger})\exp[-\tau(l_1-l_1^{\dagger})]\,\mathrm{d}l_1^{\dagger}\cos(\psi_{21})\sin(\theta)\,\mathrm{d}\theta\\
&\qquad+\int_{\theta_2'(x)}^{\theta_2(x)}\int_0^{l_2}T^4(l_2^{\dagger})\exp[-\tau(l_2-l_2^{\dagger})]\,\mathrm{d}l_2^{\dagger}\cos(\psi_{22})\sin(\theta)\,\mathrm{d}\theta\\
&\qquad+\int_{\theta_2(x)}^{\theta_1(x)}\int_0^{l_3}T^4(l_3^{\dagger})\exp[-\tau(l_3-l_3^{\dagger})]\,\mathrm{d}l_3^{\dagger}\cos(\psi_{23})\sin(\theta)\,\mathrm{d}\theta\Bigg]\Bigg\}\,\mathrm{d}\alpha\Bigg\}
\end{aligned}
\tag{47}
$$

The flux incoming from the side wall is:

$$
\begin{aligned}
&\mathbf{q}_R\cdot(-\mathbf{e}_r)|_{b3}\\
&\quad=\varepsilon_{i3}\Bigg\{T_{b3}^4-\frac{2}{\pi}\int_{\pi/2}^{\pi}\Bigg\{\int_{\theta_1(x)}^{\pi}\left[T_{b1^*}^4-\frac{1-\varepsilon_{i1^*}}{\varepsilon_{i1^*}}\mathbf{q}_R\cdot(-\mathbf{n}_{b1^*})\right]\exp(-\tau l_1)\cos(\psi_{r1})\sin(\theta)\,\mathrm{d}\theta\\
&\qquad+\int_0^{\theta_2(x)}\left[T_{b2^*}^4-\frac{1-\varepsilon_{i2^*}}{\varepsilon_{i2^*}}\mathbf{q}_R\cdot(-\mathbf{n}_{b2^*})\right]\exp(-\tau l_2)\cos(\psi_{r2})\sin(\theta)\,\mathrm{d}\theta\\
&\qquad+\int_{\theta_2(x)}^{\theta_1(x)}\left[T_{b3^*}^4-\frac{1-\varepsilon_{i3^*}}{\varepsilon_{i3^*}}\mathbf{q}_R\cdot(-\mathbf{e}_r)|_{b3^*}\exp(-\tau l_3)\cos(\psi_{r3})\sin(\theta)\,\mathrm{d}\theta\right.
\end{aligned}
$$

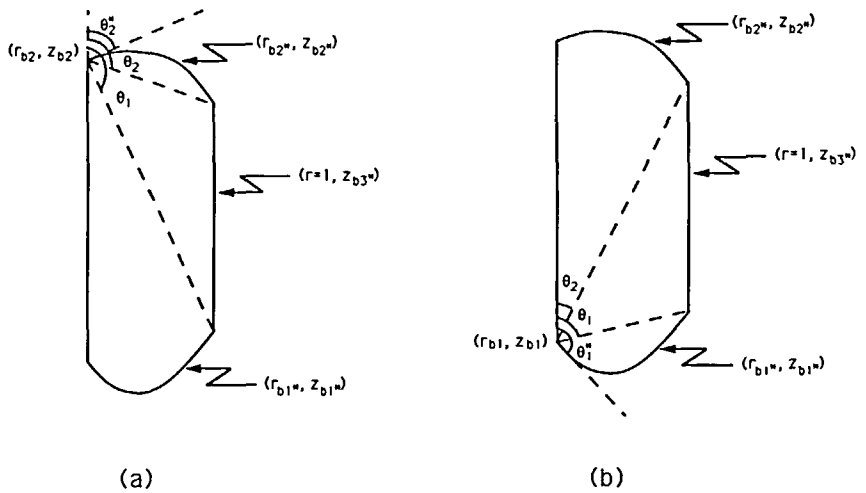

Figure 16 A constant α plane viewed from the side, for the case where the evaluation point lies on the (a) top boundary *b*2, (b) bottom boundary *b*1

$$+\tau\Bigg[\int_{\theta_1(x)}^{\pi}\int_0^{l_1} T^4(l_1^\dagger)\exp[-\tau(l_1-l_1^\dagger)]\,\mathrm{d}l_1^\dagger\cos(\psi_{r1})\sin(\theta)\,\mathrm{d}\theta$$
$$+\int_0^{\theta_2(x)}\int_0^{l_2} T^4(l_2^\dagger)\exp[-\tau(l_2-l_2^\dagger)]\,\mathrm{d}l_2^\dagger\cos(\psi_{r2})\sin(\theta)\,\mathrm{d}\theta$$
$$+\int_{\theta_2(x)}^{\theta_1(x)}\int_0^{l_3} T^4(l_3^\dagger)\exp[-\tau(l_3-l_3^\dagger)]\,\mathrm{d}l_3^\dagger\cos(\psi_{r3})\sin(\theta)\,\mathrm{d}\theta\Bigg]\Bigg\}\,\mathrm{d}\alpha\Bigg\} \tag{48}$$

In the equations above, the * superscript distinguishes surface quantities which vary with solid angle. The integration limits, θ_1^* and θ_2^* (see *Figure 16*) also depend on the point at which $\mathbf{q}_R\cdot(-\mathbf{n}_{b1})$ or $\mathbf{q}_R\cdot(-\mathbf{n}_{b2})$ are evaluated. However, these quantities do not need to be explicitly calculated, since the variable of integration is changed from θ to y (see Appendix B), and these limits are transformed from $\theta=\theta_j^*$ $(j=1,2)$ to $y=0$, and from $\theta=\theta_j$ $(j=1,2)$ to $y=(\sin\phi_z)/(\sin\alpha)$. The direction cosines $(\cos(\psi_{kj}), j=1,2,3; k=1,2,r)$ are evaluated with (30) and (31), together with the expression for $\mathbf{n}_{bj^*}$, $(j=1,2)$,

$$\mathbf{n}_{bj^*}=(-1)^j\frac{\mathbf{e}_z-\dfrac{\mathrm{d}z_{bj^*}}{\mathrm{d}r_{bj^*}}\mathbf{e}_r}{\sqrt{\left[1+\left(\dfrac{\mathrm{d}z_{bj^*}}{\mathrm{d}r_{bj^*}}\right)^2\right]}} \tag{49}$$

All other parameters in these equations follow the definitions employed in (29).

APPENDIX B

Choice of integration variables

An appropriate choice of integration variables must be made to make the evaluation of the radiation integrals feasible. This choice should allow all expressions in the integrand to be

evaluated explicitly and should be easily related to the system geometry. Below, we detail our choices.

We employ a new variable y to be used as the integration variable instead of θ for evaluating all integrals viewing the top and bottom of the enclosure, i.e. for $j = 1, 2$ (see *Figure 5*). Without this transformation, the integrals are implicit. From any point in space (r, z), we determine ray lengths, l_1 and l_2, in the following manner. The radial coordinate of the point of intersection between the ray and the boundary is determined by:

$$r_b^2 = r^2 + y^2 + 2yr\cos(\alpha) \tag{50}$$

which is derived from the law of cosines. The boundary axial coordinate is determined directly from $z_{bj} = z_{bj}(r_{bj})$ $(j = 1, 2)$, which is a known relation from the system geometry. The ray length $(l_j, j = 1, 2)$ is determined by:

$$l_j^2 = (z - z_{bj})^2 + y^2 \tag{51}$$

In addition, the colatitude θ can be calculated as,

$$\theta = \arccos\left[\frac{(z_{bj} - z)}{l_j}\right] \tag{52}$$

The limits of integration are also transformed: for $j = 1$,

$$\theta_1 \leqslant \theta \leqslant \pi \rightarrow \frac{\sin\phi_z}{\sin\alpha} \geqslant y \geqslant 0 \tag{53}$$

and, for $j = 2$,

$$0 \leqslant \theta \leqslant \theta_2 \rightarrow 0 \leqslant y \leqslant \frac{\sin\phi_z}{\sin\alpha} \tag{54}$$

The change of variable from θ to y also requires the inclusion of the one-dimensional Jacobian of transformation to the new integral, given by:

$$\frac{\mathrm{d}\theta}{\mathrm{d}y} = \frac{\cos^2(\theta)}{(z_{bj} - z)}\left\{1 - \frac{y\dfrac{\mathrm{d}z_{bj}}{\mathrm{d}r_{bj}}}{r_{bj}(z_{bj} - z)}[y + r\cos(\alpha)]\right\} \tag{55}$$

For integrals viewing the side wall $(j = 3)$, the integrals remain explicit in colatitude θ. In this case, the ray length l_3 is given by:

$$l_3 = \frac{\sin(\phi_z)}{\sin(\alpha)\sin(\theta)} \tag{56}$$

The axial coordinates of the intersection of the ray with the boundary are given by:

$$z_{b3} = z + l_3\cos(\theta) \qquad r_{b3} = 1 \tag{57}$$

For all integrals, the evaluation of terms along the ray direction depends on relating the path distance $l_j^\dagger$ to the cylindrical coordinates $r(l_j^\dagger)$ and $z(l_j^\dagger)$. These are computed with:

$$r(l_j^\dagger)^2 = r^2 + [\Delta l_j^\dagger \sin(\theta)]^2 + 2\Delta l_j^\dagger r\sin(\theta)\cos(\alpha) \tag{58}$$

and

$$z(l_j^\dagger) = z + \Delta l_j^\dagger\cos(\theta) \tag{59}$$

where $\Delta l_j^\dagger = l_j - l_j^\dagger$ and $j = 1, 2, 3$.

APPENDIX C

Numerical evaluation of the radiation integrals

There are three major issues in the numerical evaluation of the radiation solid angle integrals. The first concerns the specific quadrature techniques employed for numerical integration. The second issue involves the self-consistent interpolation of the temperature field at those quadrature points. The final issue concerns simplifications which can be implemented when attenuation from the exponential term in the integrand is significant. We discuss these issues below.

Consistent with the standard evaluation techniques for the Galerkin weighted residuals, we require the evaluation of the solid angle radiation integrals at each finite element quadrature point. At these points (r and z known), we define the localized spherical coordinate system defined in *Figures 4* and *5* and employ a repeated Gaussian quadrature technique to evaluate the solid angle radiation integrals. (We define repeated Gaussian quadrature here as standard Gaussian quadrature applied over each of several subdomains.) Specifically, the longitude α, which ranges from 0 to π, is divided into segments, and within each segment this angle is further discretized using Gauss–Legendre quadrature spacings. At each α quadrature point, a meridional plane is defined (see *Figure 5b*), which is discretized in the θ coordinate. This is done in the three separate regions described earlier. Within the region $\theta_2 < \theta < \theta_1$, which is bounded by the side wall, the angle θ is divided into segments. Within each segment, the angle is further discretized using the above-mentioned quadrature rule. In the other two regions, the colatitude θ is not directly discretized, rather the spatial variable y is discretized with the same approach as the discretization of α. The transformation of variables from θ to y, which is described in Appendix B, is not necessary when the geometry of the top and bottom boundaries is of a form that allows for explicit integration while discretizing θ directly (e.g. a finite right circular cylinder). Finally the ray length (l_j^i) is discretized, again in a repeated quadrature scheme as described above.

The quadrature scheme described above results in a large set of spatial points at which temperatures or fluxes must be determined. We determine these values from the finite element representations, (15) and (20). In the general case, this is not a trivial matter. The finite element basis functions are defined using a local non-linear isoparametric mapping for each element. The isoparametric mapping consists of the element-by-element transformation of a coordinate system (ξ, η), in which the element is a square, $(-1 \leqslant \xi \leqslant 1,\ -1 \leqslant \eta \leqslant 1)$, into the (r, z) coordinate system (see *Figure 17*). The two coordinate systems are related via the following equation,

$$r = \sum_{i=1}^{9} r_i \phi^i(\xi, \eta) \qquad z = \sum_{i=1}^{9} z_i \phi^i(\xi, \eta) \tag{60}$$

where r_i and z_i are the nodal coordinate values. The local forms of the global basis functions, $\{\Phi^i(r, z)\}$ and $\{\Gamma^i(x)\}$, are given by $\{\phi^i(\xi, \eta)\}$ $(i = 1, \ldots, 9)$ and $\{\gamma^i(\xi)\}$ $(i = 1, \ldots, 3)$ respectively and are tabulated elsewhere[73]. Finding the value of a field quantity at an arbitrary point in the domain is usually a time-consuming numerical operation, since the inverse mapping (from (r, z) to (ξ, η)) is not generally analytical. Fortunately, by careful construction of the finite element mesh, it is possible to find an analytical inverse mapping.

Our procedure to rigorously interpolate the value of a field variable from the finite element representation is as follows. Once a point is specified, i.e. the global coordinates (r, z) are known, the element in which the point rests is identified, and then the global coordinates are transformed into the local coordinates (ξ, η) using the inverse of the mapping (60). If the mesh comprises elements whose vertical sides are parallel to the z-axis (as is the case for our problems, see *Figure 17*), it is possible to do the elemental search in a simple, two-step operation. First, the appropriate column of elements (all sharing the same radial-coordinate values) is identified, and then the

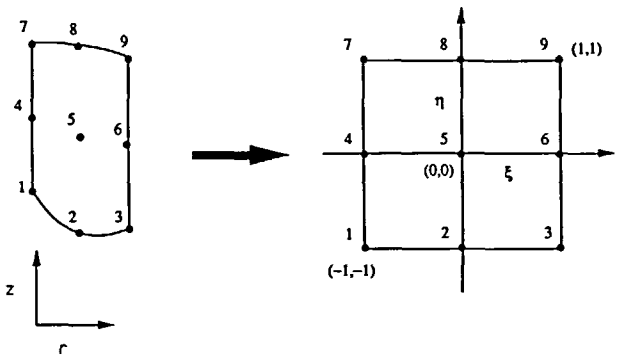

Figure 17 Schematic of inverse isoparametric mapping, from global coordinates (r, z) to local coordinates (ξ, η)

appropriate element is located via a search in the axial direction. We next employ the following inverse mapping:

$$\xi = \frac{2(r - r_1)}{\Delta r} - 1 \tag{61}$$

$$\eta = \frac{(z - c)}{b} \tag{62}$$

where

$$\Delta r \equiv r_3 - r_1 \tag{63}$$

$$c \equiv [\tfrac{1}{2}(z_4 + z_6) - z_5]\xi^2 + \tfrac{1}{2}(z_6 - z_4)\xi + z_5 \tag{64}$$

$$b \equiv \tfrac{1}{2}[\tfrac{1}{2}(z_7 - z_1 + z_9 - z_3) + z_2 - z_8]\xi^2 + \tfrac{1}{4}(z_1 - z_3 - z_7 + z_9)\xi + \tfrac{1}{2}(z_8 - z_2) \tag{65}$$

The following restrictions must be implemented in the mesh generating procedure for this transformation to hold:

$$r_1 = r_4 = r_7 \tag{66}$$

$$r_2 = r_5 = r_8 = \frac{r_1 + r_3}{2} \tag{67}$$

$$r_3 = r_6 = r_9 \tag{68}$$

$$z_4 = \tfrac{1}{2}(z_1 + z_7) \tag{69}$$

$$z_5 = \tfrac{1}{2}(z_2 + z_8) \tag{70}$$

$$z_6 = \tfrac{1}{2}(z_3 + z_9) \tag{71}$$

When applying the Swartz–Wendroff approximation, one need not evaluate the temperature at (r, z), rather, one must calculate the value of the finite element basis functions at this point. It is, however, still necessary to locate the element containing the point of interest and to invert the isoparametric mapping as outlined above.

When the domain is optically thick (i.e. $aR \gg 1$ or $aL \gg 1$), the rapid decay of the exponentials in the radiative terms calls for a change of numerical strategy. We apply certain 'cut-off' criteria to decide when it is appropriate to ignore the contribution of certain terms in the integral.

In the calculations presented here, volume terms (or line integrals) were truncated at an optical distance of $\tau(l - l') = 20$. The volume terms were evaluated according to the following rule:

$$\int_{\Omega=0}^{4\pi}\int_{0}^{l} T^4(l')\exp[-\tau(l-l')]\,dl'\cos(\psi)\,d\Omega$$

$$\approx \begin{cases} \displaystyle\int_{\Omega=0}^{4\pi}\int_{0}^{l} T^4(l')\exp[-\tau(l-l')]\,dl'\cos(\psi)\,d\Omega & \tau l < 20 \\ \displaystyle\int_{\Omega=0}^{4\pi}\int_{l-20/\tau}^{l} T^4(l')\exp[-\tau(l-l')]\,dl'\cos(\psi)\,d\Omega & \tau l > 20 \end{cases} \tag{72}$$

For optically thick cases, this procedure results in significant computational savings with no significant loss in accuracy.

For surface terms in (29), i.e. the first three terms, we employ two cut-off criteria for deciding when to ignore these terms. First, if the minimum optical distance τl_j $(j = 1, 2, 3)$ to one of the three boundaries is larger than some critical value, then the surface contributions from *that* boundary should be neglected. If the surface integral is not to be neglected, then a second cut-off criterion will determine the limits of the integrals of these surface terms.

Evaluating and applying these cut-off criteria to the surface terms is not always straightforward. We first estimate the minimum distance to each of the three surfaces from the point of interest. The distance to the side surface $L3$ is always given by a line in the plane $\alpha = 0$, and is

$$L3 = \begin{cases} l_3(\theta_1(\alpha=0)) & z \leqslant z_{b3}(\theta_1(\alpha=0)) \\ 1 - r & z_{b3}(\theta_1(\alpha=0)) < z < z_{b3}(\theta_2(\alpha=0)) \\ l_3(\theta_2(\alpha=0)) & z \geqslant z_{b3}(\theta_2(\alpha=0)) \end{cases} \tag{73}$$

The distances to the top and bottom surfaces is difficult to calculate, since the surfaces may be curved. For surfaces which are relatively flat, these distances ($L1$ and $L2$) are often well-approximated by the axial distance between the point of interest and these boundaries, so that,

$$L1 \approx z - z_{b1}(r) \tag{74}$$

and

$$L2 \approx z_{b2}(r) - z \tag{75}$$

Next we check to see if each surface is too far away (optically). The cut-off distance that was used in this study was on the order of 20–30, so that if τLj $(j = 1, 2, 3)$ proved to be larger than this value, the complete surface term was discarded. If the surface terms were not discarded, a second criterion was invoked. This entailed truncating (when necessary) the limits of the solid angle integrals of the surface terms in a manner which would keep $\tau(l_j - Lj)$ $(j = 1, 2, 3)$ below the value of the second criterion ($\mathcal{O}(20)$). In the case of $j = 3$ this involved possible truncation both in α and in θ. When $j = 1, 2$ truncation was considered only in θ, since the minimum distance from (r, z) to the top and bottom surfaces, within a plane of constant α, is independent of α and is therefore equal to $Lj, j = 1, 2$.

APPENDIX D

Geometric factors from the Swartz–Wendroff approximation

The matrices in (35) and (37) are determined using the following relations. For the matrix **A**,

$$A_{ij} = \frac{2}{\pi}\tau \int_D \nabla\Phi^i(r,z)\cdot\Bigg\{\int_0^{\pi} \times\Bigg[\int_{\theta_1(\alpha)}^{\pi}\int_0^{l_1} \Phi^j(l_1^{\dagger})\exp[-\tau(l_1-l_1^{\dagger})]\,\mathrm{d}l_1^{\dagger}[\cos(\psi_{r1})\mathbf{e}_r+\cos(\psi_{z1})\mathbf{e}_z]\sin(\theta)\,\mathrm{d}\theta + \int_0^{\theta_2(\alpha)}\int_0^{l_2} \Phi^j(l_2^{\dagger})\exp[-\tau(l_2-l_2^{\dagger})]\,\mathrm{d}l_2^{\dagger}[\cos(\psi_{r2})\mathbf{e}_r+\cos(\psi_{z2})\mathbf{e}_z]\sin(\theta)\,\mathrm{d}\theta + \int_{\theta_2(\alpha)}^{\theta_1(\alpha)}\int_0^{l_3} \Phi^j(l_3^{\dagger})\exp[-\tau(l_3-l_3^{\dagger})]\,\mathrm{d}l_3^{\dagger}[\cos(\psi_{r3})\mathbf{e}_r+\cos(\psi_{z3})\mathbf{e}_z]\sin(\theta)\,\mathrm{d}\theta\Bigg]\mathrm{d}\alpha\Bigg\}\mathrm{d}V \tag{76}$$

where $i,j = 1,\ldots,N_T$.

Coefficients of **B** are given by,

$$B_{i,j} = \frac{2}{\pi}\int_D \nabla\Phi^i(r,z)\cdot\Bigg\{\int_0^{\pi}\Bigg[\int_{\theta_1(\alpha)}^{\pi} \Gamma^j(r_{b1};z_{b1})\exp(-\tau l_1)[\cos(\psi_{r1})\mathbf{e}_r+\cos(\psi_{z1})\mathbf{e}_z]\sin(\theta)\,\mathrm{d}\theta + \int_0^{\theta_2(\alpha)} \Gamma^j(r_{b2};z_{b2})\exp(-\tau l_2)[\cos(\psi_{r2})\mathbf{e}_r+\cos(\psi_{z2})\mathbf{e}_z]\sin(\theta)\,\mathrm{d}\theta + \int_{\theta_2(\alpha)}^{\theta_1(\alpha)} \Gamma^j(1;z_{b3})\exp(-\tau l_3)[\cos(\psi_{r3})\mathbf{e}_r+\cos(\psi_{z3})\mathbf{e}_z]\sin(\theta)\,\mathrm{d}\theta\Bigg]\mathrm{d}\alpha\Bigg\}\mathrm{d}V \tag{77}$$

where $i = 1,\ldots,N_T$ and $j = 1,\ldots,N_{Tb}$, the number of nodes on the part of the boundary where a flux condition is given (∂D_f).

The matrix **C** has entries of the following form,

$$C_{ij} = -\frac{2}{\pi}\int_D \nabla\Phi^i(r,z)\cdot\Bigg\{\int_0^{\pi} \times\Bigg[\int_{\theta_1(\alpha)}^{\pi} \Gamma^j(r_{b1};z_{b1})\frac{1-\varepsilon_{i1}}{\varepsilon_{i1}}\exp(-\tau l_1)[\cos(\psi_{r1})\mathbf{e}_r+\cos(\psi_{z1})\mathbf{e}_z]\sin(\theta)\,\mathrm{d}\theta + \int_0^{\theta_2(\alpha)} \Gamma^j(r_{b2};z_{b2})\frac{1-\varepsilon_{i2}}{\varepsilon_{i2}}\exp(-\tau l_2)[\cos(\psi_{r2})\mathbf{e}_r+\cos(\psi_{z2})\mathbf{e}_z]\sin(\theta)\,\mathrm{d}\theta + \int_{\theta_2(\alpha)}^{\theta_1(\alpha)} \Gamma^j(1;z_{b3})\frac{1-\varepsilon_{i3}}{\varepsilon_{i3}}\exp(-\tau l_3)[\cos(\psi_{r3})\mathbf{e}_r+\cos(\psi_{z3})\mathbf{e}_z]\sin(\theta)\,\mathrm{d}\theta\Bigg]\mathrm{d}\alpha\Bigg\}\mathrm{d}V \tag{78}$$

where $i = 1,\ldots,N_T$ and $j = 1,\ldots,N_q$, the number of nodes on the part of the boundary where a Dirichlet condition is given (∂D_d).

Finally, the coefficients of **E** are:

$$E_{i,j} = -\frac{8N}{\tau\pi}\int_D \nabla\Phi^i(r,z)\cdot\Bigg\{\int_0^{\pi} \times\Bigg[\int_{\theta_1(z)}^{\pi} \nabla\Phi^j(r_{b1},z_{b1})\cdot(-\mathbf{n}_{b1})\frac{1-\varepsilon_{i1}}{\varepsilon_{i1}}\exp(-\tau l_1)[\cos(\psi_{r1})\mathbf{e}_r+\cos(\psi_{z1})\mathbf{e}_z]\sin(\theta)\,d\theta + \int_0^{\theta_2(z)} \nabla\Phi^j(r_{b2},z_{b2})\cdot(-\mathbf{n}_{b2})\frac{1-\varepsilon_{i2}}{\varepsilon_{i2}}\exp(-\tau l_2)[\cos(\psi_{r2})\mathbf{e}_r+\cos(\psi_{z2})\mathbf{e}_z]\sin(\theta)\,d\theta + \int_{\theta_2(z)}^{\theta_1(z)} \nabla\Phi^j(1,z_{b3})\cdot(-\mathbf{e}_r)\frac{1-\varepsilon_{i3}}{\varepsilon_{i3}}\exp(-\tau l_3)[\cos(\psi_{r3})\mathbf{e}_r+\cos(\psi_{z3})\mathbf{e}_z]\sin(\theta)\,d\theta\Bigg]d\alpha\Bigg\}dV \tag{79}$$

where $i = 1, \ldots, N_T$, while out of the set of basis functions $\{\Phi^{(j)}\}$, $j = 1, \ldots, N_T$, one should only consider those that are associated with the boundary nodes on ∂D_f. This is because the matrix **E** is derived from terms involving temperature gradients on ∂D_f.

The vectors employed in the Swartz–Wendroff approximation are calculated as follows,

$$F_i = -\frac{2}{\pi}\int_D \nabla\Phi^i(r,z)\cdot\Bigg\{\int_0^{\pi} \times\Bigg[\int_{\theta_1(z)}^{\pi} \mathbf{q}_b\cdot(-\mathbf{n}_{b1})\frac{1-\varepsilon_{i1}}{\varepsilon_{i1}}\exp(-\tau l_1)[\cos(\psi_{r1})\mathbf{e}_r+\cos(\psi_{z1})\mathbf{e}_z]\sin(\theta)\,d\theta + \int_0^{\theta_2(z)} \mathbf{q}_b\cdot(-\mathbf{n}_{b2})\frac{1-\varepsilon_{i2}}{\varepsilon_{i2}}\exp(-\tau l_2)[\cos(\psi_{r2})\mathbf{e}_r+\cos(\psi_{z2})\mathbf{e}_z]\sin(\theta)\,d\theta + \int_{\theta_2(z)}^{\theta_1(z)} \mathbf{q}_b\cdot(-\mathbf{e}_r)|_{b3}\frac{1-\varepsilon_{i3}}{\varepsilon_{i3}}\exp(-\tau l_3)[\cos(\psi_{r3})\mathbf{e}_r+\cos(\psi_{z3})\mathbf{e}_z]\sin(\theta)\,d\theta\Bigg]d\alpha\Bigg\}dV \tag{80}$$

and

$$K_i = \frac{2}{\pi}\int_D \nabla\Phi^i(r,z)\cdot\Bigg\{\int_0^{\pi}\Bigg[\int_{\theta_1(z)}^{\pi} T_{b1}^4\exp(-\tau l_1)[\cos(\psi_{r1})\mathbf{e}_r+\cos(\psi_{z1})\mathbf{e}_z]\sin(\theta)\,d\theta + \int_0^{\theta_2(z)} T_{b2}^4\exp(-\tau l_2)[\cos(\psi_{r2})\mathbf{e}_r+\cos(\psi_{z2})\mathbf{e}_z]\sin(\theta)\,d\theta + \int_{\theta_2(z)}^{\theta_1(z)} T_{b3}^4\exp(-\tau l_3)[\cos(\psi_{r3})\mathbf{e}_r+\cos(\psi_{z3})\mathbf{e}_z]\sin(\theta)\,d\theta\Bigg]d\alpha\Bigg\}dV \tag{81}$$

where $i = 1, \ldots, N_T$. The quantities $(\mathbf{q}_b\cdot(-\mathbf{n}_{bk})$ and T_{bk}, $k = 1, 2, 3)$ are supplied as boundary conditions.

The one-dimensional Galerkin weighted integral of the last six terms in (46)–(48) over the boundary ∂D_d together with the Swartz–Wendroff approximation are used to determine the matrices and vectors in (36) and (38). The details are analogous to those shown above and will therefore not be presented here.